Radar-Derived Statistics of Convective Storms in Southeast Queensland

JUSTIN R. PETER

International Centre for Applied Climate Sciences, University of Southern Queensland, Toowoomba, Queensland, Australia

MICHAEL J. MANTON

School of Mathematical Sciences, Monash University, Clayton, Victoria, Australia

RODNEY J. POTTS AND PETER T. MAY

Centre for Australian Weather and Climate Research, Melbourne, Victoria, Australia

SCOTT M. COLLIS

Environmental Science Division, Argonne National Laboratory, Argonne, Illinois

LOUISE WILSON

School of Mathematical Sciences, Monash University, Clayton, Victoria, Australia

(Manuscript received 8 August 2013, in final form 24 April 2015)

ABSTRACT

The aim of this study is to examine the statistics of convective storms and their concomitant changes with thermodynamic variability. The thermodynamic variability is analyzed by performing a cluster analysis on variables derived from radiosonde releases at Brisbane Airport in Australia. Three objectively defined regimes are found: a dry, stable regime with mainly westerly surface winds, a moist northerly regime, and a moist trade wind regime. S-band radar data are analyzed and storms are identified using objective tracking software [Thunderstorm Identification, Tracking, Analysis, and Nowcasting (TITAN)]. Storm statistics are then investigated, stratified by the regime subperiods. Convective storms are found to form and maintain along elevated topography. Probability distributions of convective storm size and rain rate are found to follow lognormal distributions with differing mean and variance among the regimes. There was some evidence of trimodal storm-top heights, located at the trade inversion (1.5–2 km), freezing level (3.6–4 km), and near 6 km, but it was dependent on the presence of the trade inversion. On average, storm volume and height are smallest in the trade regime and rain rate is largest in the westerly regime. However, westerly regime storms occur less frequently and have shorter lifetimes, which were attributed to the enhanced stability and decreased humidity profiles. Furthermore, time series of diurnal rain rate exhibited early morning and midafternoon maxima for the northerly and trade regimes but were absent for the westerly regime. The observations indicate that westerly regime storms are primarily driven by large-scale forcing, whereas northerly and trade wind regime storms are more responsive to surface characteristics.

1. Introduction

Southeast Queensland (SE Qld) in Australia experienced a protracted drought that began in early 2001 and continued through to the end of 2009, during which dam levels fell to unprecedented lows of about 15% capacity.[1] Because of the severity of the drought, the Queensland state government initiated a study into their water resources, one component of which was the

Corresponding author address: Justin R. Peter, International Centre for Applied Climate Science (ICACS), West St., Toowoomba, QLD, 4350, Australia.
E-mail: justin.peter@usq.edu.au

[1] The region subsequently experienced severe flooding in February 2011, which replenished dam levels to near capacity.

DOI: 10.1175/JAMC-D-13-0347.1

Queensland Cloud Seeding Research Project (QCSRP; Tessendorf et al. 2012). In addition, the Australian Bureau of Meteorology (the Bureau) was commissioned to undertake a climatology of precipitation with a particular focus on convective storms in SE Qld, the results of which are presented in this paper. The main goals of this work are to 1) determine where convective storms are most likely to occur in SE Qld, 2) examine thermodynamic atmospheric profiles to assess the large-scale conditions conducive to convective storm formation, and 3) investigate how important properties such as storm size, height, and rain rate vary under differing thermodynamic situations.

Southeast Qld is in the subtropics and has coastline to the east and the mountains of the Great Dividing Range, which rise to an altitude of nearly 1000 m, to the west. The region is particularly prone to severe convective storms and the associated hazards of flash floods, strong winds, hail damage, and, occasionally, tornadoes. The predictability of convective storms on scales of a few hours (nowcasting) and their resulting development is a challenging problem and has been the focus of numerical (Sun et al. 2014) and observational (Browning et al. 2007; Weckwerth et al. 2004; Wulfmeyer et al. 2011) studies. The observations from intensive field programs have been invaluable in helping ascertain the predominant factors that lead to convective storm initiation. These include convergence lines (e.g., sea breezes), irregular orographic heating, and thin stable layers [or "lids" in the terminology of Browning et al. (2007)]. Weckwerth et al. (2011) conducted a climatological study of convective initiation locations in southwestern Germany during the Convective and Orographically-induced Precipitation Study (Wulfmeyer et al. 2011) using two-dimensional radar composites. They found that convective storms formed preferentially over the mountains and were strongly regulated by diurnal heating. Similar conclusions were reached by Bellon and Zawadzki (2003) who used radar observations of vertically integrated liquid water content as a proxy to determine the geographical coverage of deep convective storms. Goudenhoofdt and Delobbe (2013) examined high-resolution volumetric radar data to conduct a 10-yr climatology of convective storms in Belgium. Their analysis considered not only convective initiation but various statistics of convective storms, such as lifetime and average probability of occurrence. Similarly, they found that regions of slightly higher convective initiation were related to orography. Further confirmation of the regulation of precipitation by orography has recently been detailed in Chen et al. (2014), who found increased convective activity on the windward slopes of mountains in south China.

As well as the nowcasting problem of convective initiation, the general morphology and spatial statistics of moist convection are also of interest. These properties can be best understood by examination of long-term observations that span several seasons. There has been a long history of examining multiyear statistics of convective storms using radar as the measurement platform (e.g., Cetrone and Houze 2006; Cifelli et al. 2007; Chen et al. 2012, 2014; Cheng and Houze 1979; Goudenhoofdt and Delobbe 2013; Houze and Cheng 1977; Johnson et al. 1999; Lopez 1976; Potts et al. 2000; Saxen et al. 2008). Many of these (e.g., Cetrone and Houze 2006; Cheng and Houze 1979; Cifelli et al. 2007; Houze and Cheng 1977; Johnson et al. 1999; Lopez 1976; Potts et al. 2000) found that properties such as the area, height, and duration of radar echoes followed lognormal distributions. Others have indicated that a better fit is supplied by a power law (e.g., Cahalan and Joseph 1989; Neggers et al. 2003; Saxen et al. 2008). Of particular importance in the tropics and subtropics is the height distribution of precipitating convective systems. Malkus and Riehl (1964) conducted one of the first studies that examined the height distribution of precipitating systems and found they were generally separated into two modes: a shallow cumulus mode confined below the trade inversion and deep precipitating systems that extended throughout the depth of the troposphere. Johnson et al. (1999) and Zuidema (1998) provided observational evidence of a third midlevel, or congestus, mode that had tops near the 0° isotherm. They attributed the formation of this mode to stable layers that form near the freezing level because of melting snow and ice particles (Haynes and Stephens 2007; Johnson et al. 1996). Recently, Kumar et al. (2013a) extended the classification to include an extra mode with tops overshooting the tropopause. In contrast, a study by May and Ballinger (2007) noted a continuous distribution of cell heights whose mode shifted toward higher values when conditioned on larger reflectivity.

The diurnal evolution of convection and precipitation is a fundamental characteristic of regional weather patterns. It is also an important parameter used to diagnose and validate numerical weather and climate models (e.g., Noda et al. 2012). In general, a precipitation maximum is found in the mid- to late afternoon with a smaller maxima sometimes present in the early morning preceding dawn (e.g., Nesbitt and Zipser 2003); however, this is also complicated by orography. In mountainous regions, for instance, East Asia, nocturnal rainfall peaks have been found in valleys and the foothills because of low-level convergence of valley breezes and sea breezes (e.g., Li et al. 2008). In some regions, the rainfall peaks show propagation toward downstream

areas (e.g., Li et al. 2008), while in others these observations are not present (e.g., Saxen et al. 2008). It has generally been found that elevated regions act as heat sources and preferential areas for the initiation of convection (e.g., Carbone et al. 2002; Weckwerth et al. 2011), although the diurnal cycle has been shown to be highly dependent on the time of year and the wind regime present (Chen et al. 2012; Keenan and Carbone 2008; May et al. 2012).

The climatology of convective storms in Australia has been mainly confined to understanding deep convection and its interaction with the monsoon near Darwin (e.g., Kumar et al. 2013b; May et al. 2008, 2012, and references contained therein). Other studies of storms in Australia have focused on extreme events (e.g., Abbs and McKinnes 2004; Matthews and Geerts 1995) because these are responsible for the majority of property damage, injury, or death. An exception was the study of Potts et al. (2000), who examined radar data from 12 thunderstorm days from one summer. They also found that convective storms formed preferentially over mountainous topography and that size and height distributions of the storms were distributed lognormally.

Since this paper is intended to provide a background climatology, we do not focus solely on extreme events but conduct our analysis on all observed storms. Analyzing all storms provides a description of a range of cloud systems and will enable the representativeness of systems chosen for future QCSRP case studies to be placed in context. This study presents statistics of convective storms via analysis of six years of radar data. We report on similar statistics as presented in previous studies (e.g., Cetrone and Houze 2006; Goudenhoofdt and Delobbe 2013; Houze and Cheng 1977; Potts et al. 2000), such as storm initiation location, storm area and volume, rain rate, and storm motion. Apart from the observations of Goudenhoofdt and Delobbe (2013), who analyzed 10 years of radar data, these studies focused on short (approximately 6–12 weeks) periods during summer, while this analysis examines storms during all seasons of the period 2000–06. Furthermore, this analysis builds on these studies as we also examine how the storm statistics vary with synoptic situation and season. In addition, we explore the distribution of convective storm-top heights and attempt to infer how it is modified during differing thermodynamic conditions. We also present observations of the diurnal cycle of convective storms under differing synoptic regimes.

The datasets employed are described in section 2. In section 3 we employ a clustering technique of radiosonde-derived variables, to classify the major synoptic regimes prevalent in SE Qld. In section 4 we evaluate statistics of storms determined from the objective storm classification methodology, Thunderstorm Identification, Tracking, Analysis, and Nowcasting (TITAN; Dixon and Weiner 1993), for the entire observational period and then extend the analysis to examine how the statistics vary under the differing synoptic regimes determined from the clustering analysis. Section 5 summarizes the main conclusions.

2. Datasets

a. *Radiosonde data*

The radiosonde data comprise the historical record of radiosonde measurements at Brisbane Airport in Queensland during the period from January 2001 to the end of March 2008. The Bureau obtains soundings twice daily (at 0000 and 1200 UTC; local time is UTC + 10 h) from balloon releases. The environment for a day was generally computed from the 0000 UTC radiosonde; however, if that sounding was not available then the relevant 1200 UTC sounding was used. The analysis was undertaken using observations interpolated to the "standard levels" from 1000 to 20 hPa. The standard levels are 1000, 925, 850, 700, 500, 400, 300, 250, 200, 150, 100, 70, 50, 30, and 20 hPa.

b. *Radar data*

The radar dataset used was obtained from the Bureau's Marburg, Queensland, radar (27.61°S, 152.54°E; see Fig. 1). It is a Weather Surveillance Radar 74S/14 that transmits 10-cm (S band) wavelength electromagnetic radiation. Nearly six years of archived data were analyzed, extending from January 2001 to the end of December 2006. The start time of January 2001 was chosen because prior to this there were inhomogeneities in data collection and archiving, while the end time was chosen to reflect conditions similar to those experienced prior to beginning QCSRP.

The Marburg radar collects a three-dimensional volume of polar data every 10 min. Each volume consists of 15 tilts ranging in elevation angles from 0.5° to 32°. The azimuthal and range resolutions of the data are 1° and 1000 m, respectively, and the beamwidth is 1.2°. The radar is located at an altitude 370 m above sea level and has a range of 256 km and a good overall view of precipitation in most directions except for some beam blockage by topography in a narrow sector to the south-southwest, where the terrain reaches an altitude of nearly 900 m (see Fig. 1). The 0.5°-elevation radar beam is at an altitude of about 670 m at 55-km range (approximately 0.5° spacing on Fig. 1) under standard refractive conditions, while that of the 1.2°-elevation beam is at an altitude of about 1160 m. A detailed beam

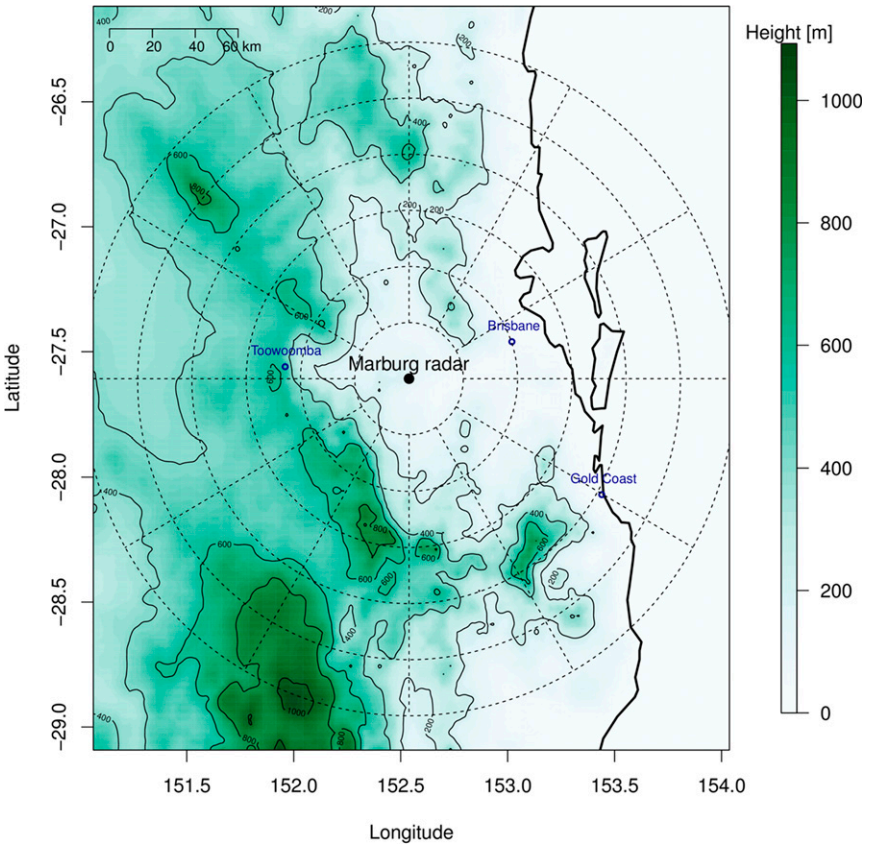

FIG. 1. The location of the Marburg radar shown on a topographic map of the SE Qld region. Marburg is at an altitude of approximately 300 m. Range rings are shown at 25-km intervals.

blockage map (not shown) indicated that the maximum loss of equivalent reflectivity (which occurred in the southwest sector) was 5.6, 2.2, 0.6, and 0.07 dBZ in the first through fourth elevation tilts (0.5°, 1.2°, 1.9°, and 2.7°, respectively). This may introduce a bias, whereby small storms in this region may not be detected until they have moved to a location where the beam blocking is less substantial. To mitigate some of the effects of clutter, the radar data have had some signal processing applied to them. A simple statistical filter is applied that identifies targets that do not vary much in amplitude from pulse to pulse and designates them clutter. However, if rain should fall over a permanent echo (PE), the received signal may include power from both rain and PE if the filter declares it as rain. The radar calibration is routinely checked against solar power measurements and the absolute error is considered to be less than 2 dBZ.

The convective storm dataset was obtained using the TITAN radar analysis tool (Dixon and Weiner 1993). TITAN can analyze both polar and Cartesian radar volume data but for this analysis we use Cartesian data. The transformation from the polar coordinate data obtained by the radar is achieved using an 8-point bilinear interpolation method, where the interpolation is performed in order, range, and azimuth and then elevation. The resulting Cartesian radar data have a horizontal domain of 460.5 × 460.5 km^2 and vertical domain of 20.25 km, where the grid spacing is 0.75 km along all axes. The interpolation scheme can introduce artifacts, especially in regions with large reflectivity gradients, (e.g., Collis et al. 2010; Zhang et al. 2005); however, Goudenhoofdt and Delobbe (2013) conducted sensitivity studies that indicated that the effect on the retrieved number of storm tracks was minimal when the vertical grid resolution was below 1 km.

The TITAN software identifies contiguous volumes of pixels that exceed a prescribed reflectivity and size threshold, which for this analysis were 35 dBZ and 30 km^3, respectively. Similar thresholds have been used in previous studies (e.g., Goudenhoofdt and Delobbe 2013; Kumar et al. 2013b; May and Ballinger 2007). Note that contiguous here applies only to grid neighbors, not linked corner pixels. The prescription of these size and

reflectivity thresholds implies that convective storms are identified, since stratiform rain is generally confined to reflectivities below 35 dBZ. The choice of a reflectivity threshold may influence storm identification and is an important parameter for TITAN. As the reflectivity threshold is increased, individual convective cores within a precipitating system will be identified as separate storms, which allows for better tracking albeit with decreased ability to track growth and decay life cycles of a storm. Alternatively, if the threshold is lowered to, for example, 30 dBZ, then a greater areal extent will be identified, enabling the entire storm life cycle to be better captured although individual reflectivity peaks within the region will not be registered (e.g., Goudenhoofdt and Delobbe 2013). The Marburg radar uses the relationship $Z = 500R^{1.3}$ to convert reflectivity Z to rain rate R, so the lowest reflectivity limit of 35 dBZ corresponds to a moderate rain rate of about 6 mm h^{-1}. Additionally, a reflectivity threshold of 55 dBZ is used by TITAN to distinguish rain from hail. The analysis in this paper was also performed using a reflectivity threshold of 45 dBZ, which had the effect of changing some values of quantities reported, but the main conclusions were not affected. The 35-dBZ threshold for defining a storm means that the storm-top height will be significantly underestimated compared to the actual cloud-top height (CTH). Other studies (e.g., Houze and Cheng 1977) have used a minimum detectable signal (MDS), dependent on the radar sensitivity, to accumulate the storm statistics. The height of the MDS may extend several kilometers above the height defined by the 35-dBZ threshold, while the CTH may extend higher again. On the other hand, prescribing a reflectivity threshold of 35 dBZ is a better indicator of storm intensity (DeMott and Rutledge 1998; Zipser and Lutz 1994) and therefore more appropriate to distinguish storms.

Once a storm has been identified, the TITAN software can track its movement by matching storms across successive radar scans using a combinatorial optimization method followed by an additional geometric algorithm to handle the splits and mergers of storms. The entire spatial and temporal history of each of these storm entries is referred to as a storm track. Two identifiers are assigned to each entry of the storm track: a simple track number where the separate elements are tracked and a complex track number where the storm is considered a single entity combining splits or merger components. For this analysis, we consider each individual entry of the storm track and refer to this as a "storm." Furthermore, we only consider storms that could be tracked over at least two successive radar volumes. The specification of a minimum lifetime has the additional benefit of reducing the effects of clutter and permanent echoes.

3. Synoptic regimes

a. *Qualitative overview of SE Qld weather*

The annual climate of SE Qld can be broadly described as consisting of "dry" and "wet" seasons. The dry season roughly comprises the months April–October, and the wet season is November–March. Southeast Qld, however, is in the subtropics and has quite a few departures from the typical wet–dry seasonal cycle prevalent farther north in the tropics. For instance, during the dry season, frontal systems associated with midlatitude cyclones traversing southern Australia penetrate far enough into the subtropics to bring appreciable rainfall to the region. Also during the dry season, intense subtropical cyclones can form off the east coast of Australia (known locally as east coast lows), which bring sustained strong winds and intense rainfall (Hopkins and Holland 1997). During the wet season, trade wind showers predominate, especially along the coastal regions. These showers, many of which reach maximum altitudes of only 4 km, regularly register reflectivities of 45–50 dBZ. The wet season is also the most likely time for the development of large, sometimes supercell, thunderstorms.

The propensity for thunderstorm formation is largely modulated by the position of the subtropical ridge and the inland trough. Instability associated with the trough will promote the formation of thunderstorms, while the position of the subtropical ridge modulates the direction of the surface winds. When the flow is from the southeast, a strong thermal and moisture inversion typical of a trade wind regime results. As the ridge propagates east, the surface winds shift northerly, resulting in increased heat and moisture fluxes. If the northerly flow coincides with an unstable atmosphere, such as surface or upper-level troughs, deep convective storms can result (Klingaman 2012). Local forecasters note that generally storms tend to form on the ranges and move toward the coastal plains.

b. *K-means clustering of sounding data*

To identify how the synoptic conditions influence storm properties, it is necessary to prescribe thermodynamic and dynamic metrics by which the synoptic meteorology can be objectively classified and compared. Several attempts have been made at using an objective classification method, utilizing differing measurements. For instance, Abbs and McKinnes (2004) defined synoptic regimes using mean sea level pressure data, while others (e.g., Connor and Bonnel 1998; Lucas and Zipser 2000; Pope et al. 2009a,b; Tudurí and Ramis 1997) have used radiosonde data. Here we take a similar approach to Pope et al. (2009a) and conduct a K-means clustering (Gong and Richman 1995; Hartigan and Wong 1979) on

TABLE 1. Variables derived from the Brisbane soundings that were used as input to the *K*-means clustering algorithm.

Variable	Description
U	Westerly wind at 850 hPa
V	Southerly wind at 850 hPa
Sh	RMS wind shear between 500 and 850 hPa
TT	$T(850) - 2T(500) - T_d(850)$ where T and T_d are the temperature and dewpoint temperature, respectively
QU	Westerly water flux up to 250 hPa
QV	Southerly water flux up to 250 hPa
TW	Total water up to 250 hPa

variables derived from 2541 radiosonde soundings obtained at Brisbane Airport. The variables chosen to represent the synoptic environment are listed in Table 1 and are calculated from the standard level sounding data. They encompass measures of the prevailing winds and moisture fluxes (*U*, *V*, QU, QV), instability [total totals (TT)], shear (Sh), and total precipitable water (TW) and combined provide a description of the propensity for rainfall. It should be noted that the *K*-means clustering is unlikely to uniquely identify conditions that are conducive to the formation of the most severe thunderstorms, primarily because of their infrequent occurrence. However, our primary focus is how the statistics of storms change under broadly classified synoptic conditions.

The seasonal cycle of the clustering variables is shown in Fig. 2.[2] The atmospheric moisture content (TW) exhibits a pronounced seasonal cycle and captures the transition from the ''wet'' season summer to the ''dry'' season winter. The atmospheric stability also shows a pronounced seasonal cycle with a more stable atmospheric profile during winter. The surface winds are mainly from the southeast during the summer, indicative of the prevailing trade wind flow, and progress to a more northwesterly flow during the winter. Moisture fluxes are enhanced during summer reflective of the oceanic origin of air masses, while the wintertime dry continental surface flow is evident in a decreased surface moisture flux.

[2] We will present box plots several times in this paper as they provide a great deal of information. The horizontal line shows the median value, while the bottom and top of the box represent the 25th and 75th percentiles. The top and bottom of the whiskers display 1.5 times the interquartile range of the data or roughly two standard deviations. Points below (above) the bottom (top) of the whiskers are designated outliers. The width of the boxes is proportional to the square root of the number of observations within the groups. Finally, the notches in the boxes give an indication of the statistical significance of the difference between the median of the samples; boxes in which the notches do not overlap have significantly different medians.

The *K*-means clustering technique requires that input variables are scaled and that the initial number of clusters be specified. All variables were scaled by subtracting the mean and dividing by the standard deviation. For the moment, we consider the use of three clusters to illustrate the relationship between the variables listed in Table 1. Specifying three clusters also has a correspondence with the qualitative description of the meteorology discussed previously. The relationships between the variables chosen for the cluster analysis when three clusters are considered are shown in Fig. 3. Each cluster can be identified as a synoptic regime: 1) one with low TW and TT, and mainly westerly to southwesterly winds (black circles); and 2) two regimes with large moisture content and instability, one with winds mainly from the northwest (red circles) and the other with winds from the southeast (green circles). While both the northwesterly and southeasterly regimes have large moisture fluxes, the northwesterly regime is slightly more unstable than that with southeasterly winds.

More clusters could have been specified, however, when the analysis was repeated with four clusters it resulted in the southeasterly cluster split into two subclusters, one with a more southerly component and the other with a more easterly component. When increased to five clusters, a cluster with properties between the northwesterly and southeasterly regimes appeared. As such, we decided that three clusters was appropriate to use as 1) the resulting clusters had a direct meteorological correspondence with the qualitative description used by operational meteorologists, and 2) increasing the number of clusters decreased the number of days assigned to each cluster, thereby degrading the statistics. A recent study by Wilson et al. (2012) completed a similar analysis using eight clusters; however, the purpose of their study was to document the synoptic regimes associated with the presence (or lack thereof) of rainfall, whereas this study seeks to document the properties of convective storms.

It is instructive to examine the seasonal cycle of the regimes to determine the time of year each is most likely to occur. Total water as a function of day of year (doy) is shown in Fig. 4. It is clear that the regime with low moisture, low instability, and southwesterly winds (black circles) occurs mainly in winter, while the others occur mainly during summer. For the rest of the paper we will adopt a naming convention for the three regimes identified by the clustering algorithm. These are 1) a *westerly* regime with low TW and TT, 2) a *trade wind* regime with mainly southeasterly winds, and 3) a *northerly* regime characterized by an unstable atmosphere and surface flows with large equivalent potential temperature. The westerly regime is also distinguished by having a surface flow that is

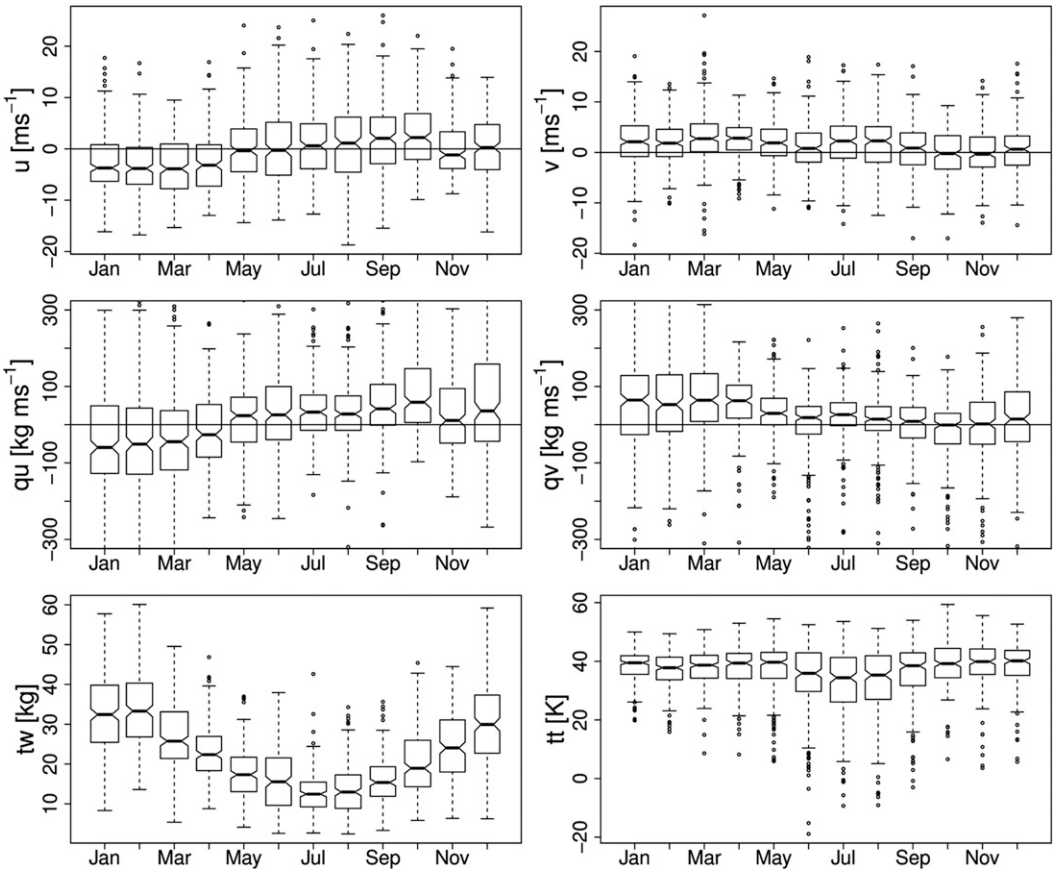

FIG. 2. Monthly-averaged seasonal variation of sounding-derived environmental variables for the period from January 2001 to March 2008. See Table 1 for a description of the variables.

continental in origin, whereas the northerly and trade regimes have oceanic surface winds. The naming convention we have adopted is one that best describes the characteristics of the cluster as a whole; however, departures are to be expected, primarily because of the statistical nature of the clustering algorithm.

A total of 2541 soundings were used for the analysis, and the relative proportion assigned to each cluster was, 26% (659), 26% (658), and 48% (1224) for the westerly, northerly, and trade regimes, respectively. However, this breakdown includes days during which no storms were measured by the radar. The total number of storms recorded over the observational radar period of 2191 days (January 2001–December 2006) was 26 227, or about 12 storms per day. During this period, a convective storm was registered by the radar on 1084 days, such that the average number of storms per day when storms were recorded was about 24. In addition, not every day on which a storm was observed could be classified by the clustering algorithm because of a lack of sufficient information in the sounding. Generally this was when the GPS failed and no wind, and hence shear, information could be derived although sometimes temperature or dewpoint readings failed. Of the 1084 days on which convective storms were present, 932 days were assigned a cluster and a total of 20 675 storms were recorded. The resulting number of days for each regime when convective storms were measured was 189/20% (westerly), 267/29% (northerly), and 476/51% (trade). In contrast, the number of storms and their respective percentages were 2507/12% (westerly), 9603/47% (northerly), and 8565/41% (trade). Therefore, the average number of storms per day in each regime was 13 (westerly), 36 (northerly), and 18 (trade). The increased number of storms (in both absolute values and relative number per day) during the northerly regime is consistent with its larger instability and total column water.

c. *Synoptic-regime thermodynamic profiles*

The regime thermodynamics are summarized in Fig. 5. The median profiles of temperature and dewpoint on a skew T–log$p$ diagram (including wind speed and direction profiles) are shown in Fig. 5a, while Fig. 5b

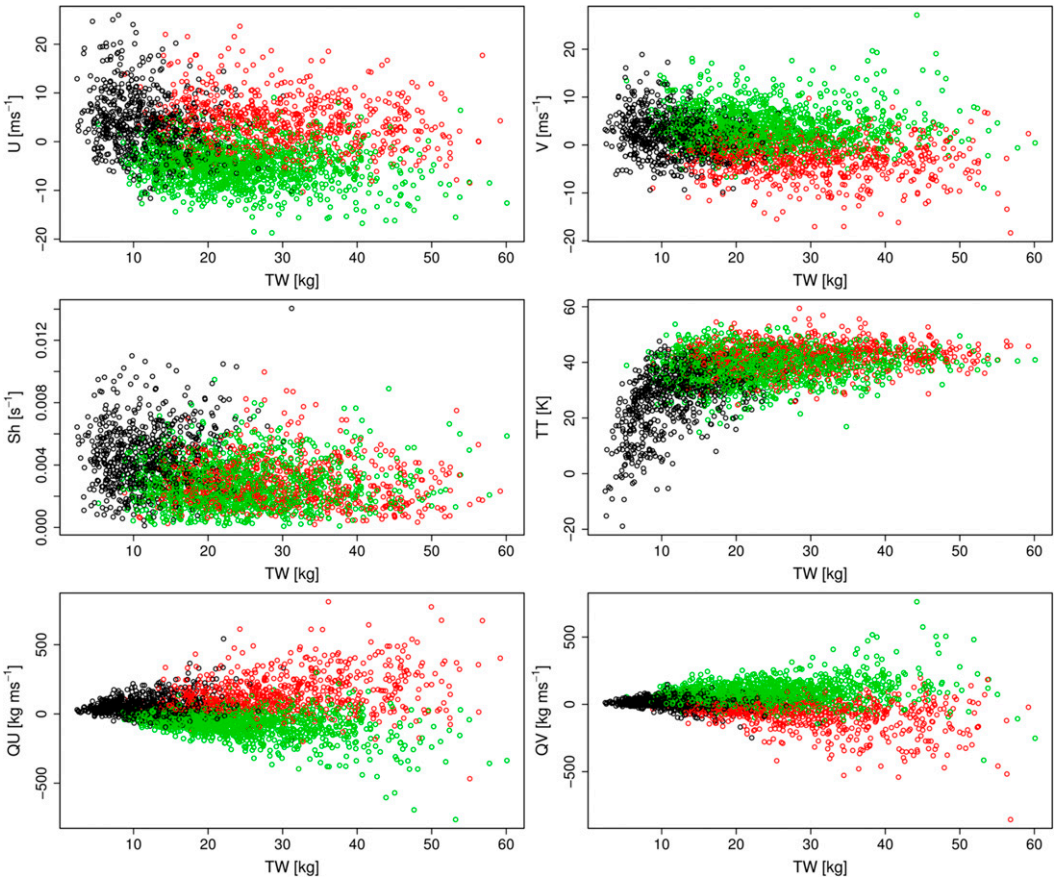

FIG. 3. Relationships between environmental variables in Table 1 with three clusters. The three clusters correspond to the following synoptic regimes: 1) a westerly regime (black circles), 2) a northwesterly regime (red circles), and 3) a southeasterly (trade) regime (green circles).

presents the derived profiles of potential temperature θ, equivalent potential temperature θ_e, and saturation equivalent potential temperature θ_{es}. The westerly regime has the least amount of directional wind shear but has a distinct mid- and upper-level jet compared to the other regimes. It is also extremely dry, exhibiting large dewpoint depressions through the mid- and upper levels. The northerly regime shows directional wind shear up to about 850 hPa, while the midlevel wind speeds are between those of the westerly and trade regimes. It is also very moist throughout the whole extent of the troposphere and has the most unstable profile. The trade regime exhibits a sounding with characteristics classic to those regions near the descending branch of the Hadley cell. In particular, despite this being a composite of many soundings, the trade inversion is evident between about 2–3 km. Additionally, southeasterly winds prevail below the inversion and westerly winds above. The wind speed shear of the trade regime is the smallest of the regimes.

The derived temperature profiles (Fig. 5b) provide extra important information about the stability profiles of the atmosphere among the three regimes. In particular, profiles of saturation equivalent potential temperature convey information on the stability when moist processes occur. The westerly regime is stable in the lowest several hundred meters of the boundary layer with a conditionally unstable layer extending to just below 2 km. A very stable layer is evident through to about 3 km above which the atmosphere is stable throughout the extent of the troposphere. The northerly regime is unstable up to about 4 km, with a shallow neutrally stable layer just below 2 km. It exhibits neutral stability up to about 7 km. The trade regime profile is very unstable in the lowest levels and a strong stable trade inversion is evident between 1.5 and 3 km (850–700 hPa) with a stability profile matching that of the northerly regime through the rest of the troposphere. There is also a dry layer associated with subsidence above the temperature inversion that extends between 750 and 600 hPa (2.5–4 km).

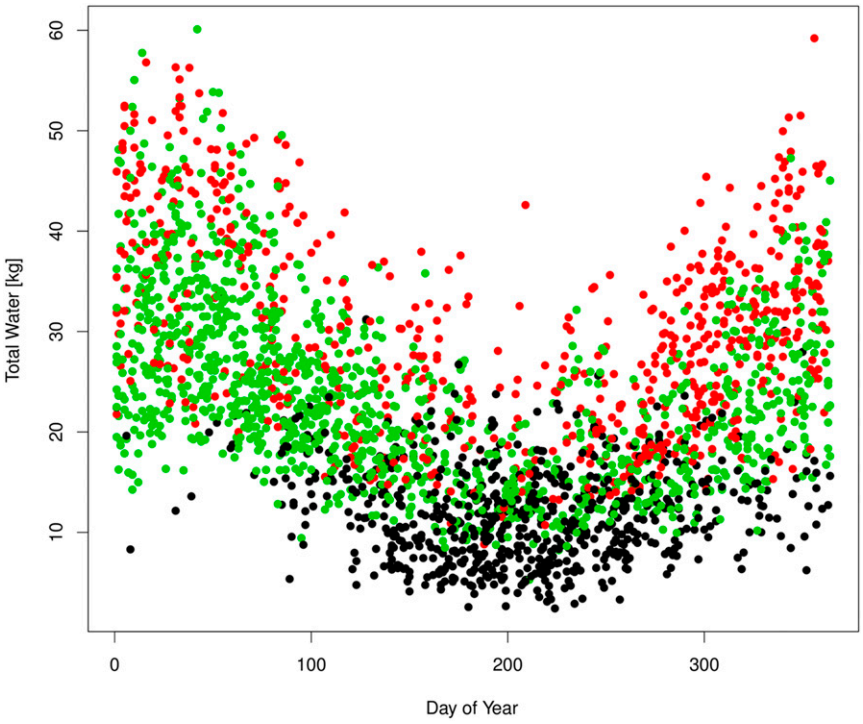

FIG. 4. Seasonal cycle of total water for the synoptic regimes determined by *K*-means clustering analysis; black is the westerly regime, red is the northerly regime, and green is the southeasterly trade wind regime.

The sounding data show that the climatological height of the freezing level is about 3.1 km for the westerly regime and 4 km for the northerly and trade regimes. Minima exist in the profiles of θ_e just below the respective freezing level indicating the presence of a dry, stable layer. The soundings also indicate the presence of three other climatological stability levels, one at the trade inversion (between 1.5 and 3 km), one in the midtroposphere between about 6 and 8 km (particularly evident in the profiles of θ_e and θ_{es}) and near the tropopause (determined by the minimum in the temperature profile) at about 12–13 km. Kumar et al. (2013a) found similar tendencies in average profiles of temperature lapse rate and we will examine the distribution of storm-top heights and their relationship to the presence of the stable inversions in section 4b.

4. Storm statistics

a. *Storm-location frequency*

The spatial distribution of 35-dBZ storm frequency is shown in Fig. 6. Each two-dimensional histogram box covers an approximate 17 km × 17 km area and the frequency represents the number of times the storm (areal) centroid was registered in that box. The frequency has been scaled by the maximum number of storms registered in any grid box across the domain. Using the areal centroid may be unrepresentative of storm location especially for large storms. Analysis of the storm area distribution (see section 4b) showed that storms with an area coverage of greater than about 1100 km^3, which represents approximately four grid boxes, contributed only a small fraction to the total number of storms, so that the spatial distribution should be representative of storm location for most storms.

At short ranges the radar is "blind" to precipitation; hence a minimum in frequency is located near the radar. Furthermore, at close distances, the radar beam may not reach storm top if the storm is above the level of the "cone of silence." Additionally, at distances greater than about 200 km from the radar, the beam height is greater than 4 km, which is approximately the height of the freezing level, so many of the shallow trade wind cumulus that are confined below this level will not be viewed by the radar. Moreover, since the width of the beam increases with distance from the radar, many storms may be smoothed over a large beam volume. For the above reasons, only observations in the range 20–130 km are considered in subsequent analysis to minimize errors in storm statistics due to beam geometry. Similar limits were used by Potts et al. (2000) and Kumar et al. (2013b).

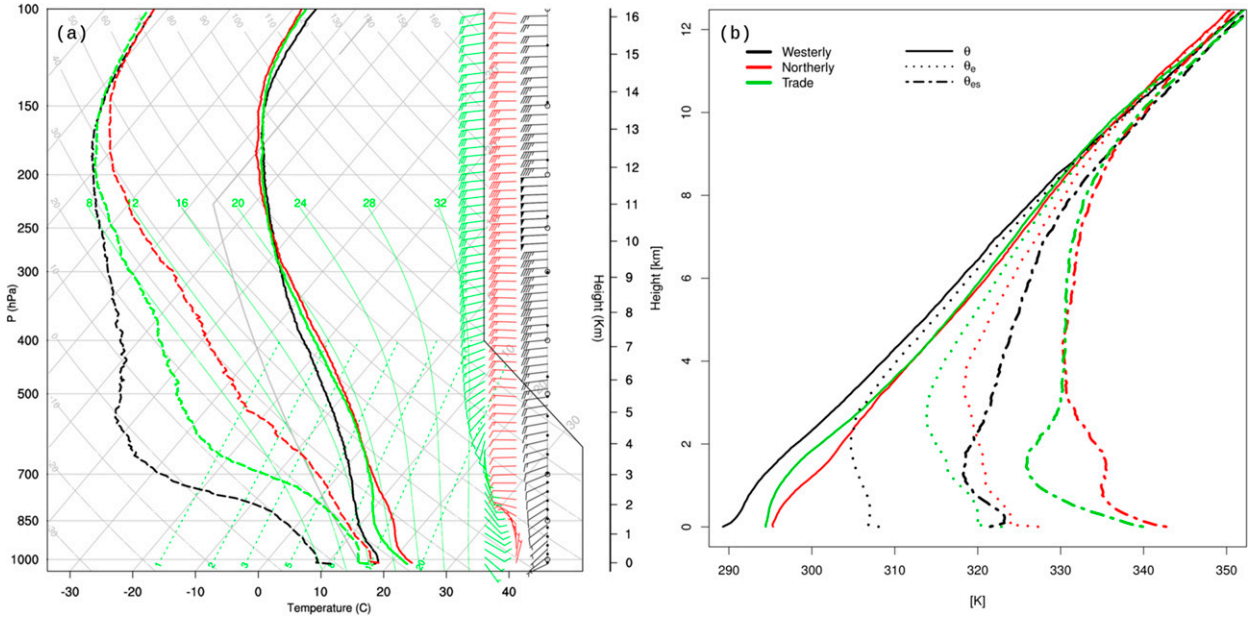

FIG. 5. (a) Skew T–log$p$ diagram of the median of temperature and dewpoint for each of the synoptic regimes identified by the K-means clustering algorithm. Wind speed and direction profiles are also shown. (b) Profiles of the median values of θ, θ_e, and θ_{es}. The regime color key is given in (b).

Figure 6a shows the spatial frequency for all 35-dBZ storms within the range-restricted domain. The total number of storms in this domain was 12 318 and of those 9296 occurred on a day that could be assigned a cluster regime. Of the 12 318 storm entries, 6634 had a unique complex track number, indicating that the remainder (5684, about 46%) of storm entries belonged to storms that had undergone a split/merger. Similarly, the number of unique simple storm tracks was calculated to be 8250, indicating that about 67% of storm entries belonged to a simple storm track with the minimum specified lifetime of 20 min (two successive radar volumes). It must be remembered, however, that a single track may have resulted from split/merger of a previous storm. Despite the problems of beam geometry and width, it is clear that the majority of storms originate on elevated topography north and south of Marburg radar. In particular, the maximum storm-location frequency occurs to the southeast where the ranges reach 500-m altitude relatively close to the coast. Figure 6b shows the location for the first storm entry on any day and indicates storms preferentially form over elevated topography especially to the south and southeast of Marburg radar. There is also an increase in initiation location at the northern island (Moreton Island, Queensland) off the coast that reaches an altitude of 280 m. These maps demonstrate the strong influence topography has in initiating and sustaining storms, either through uplift or differential heating. Similar observations were obtained by Matthews and Geerts (1995) and Potts et al. (2000) for storms in the Sydney, New South Wales, region (Australia) and Lang et al. (2007) in the Gulf of California. Figures 6c–e show the spatial frequency of storm occurrence for each of the synoptic clusters identified in section 3. All regimes show an increased propensity for storms to form north and south of the radar indicating the importance of topography in generating and sustaining storms regardless of the prevailing flow. Also, the trade regime exhibits a slight increase in storm location over the ocean compared to the other regimes.

b. *Storm size and rain rate*

Previous studies have shown that the frequency distribution of precipitation area (or an equivalent horizontal dimension) can be represented by a truncated lognormal distribution (e.g., Lopez 1976, 1977; Potts et al. 2000; Cifelli et al. 2007).[3] The probability distribution function (pdf) of convective precipitation area[4] in the range-restricted domain is plotted in Fig. 7a,

[3] Lopez (1977) noted that lognormal distributions arise as a result of a variate that is subject to the law of proportionate effects.

[4] Here, precipitation area refers to the area occupied in the lowest level of the Cartesian grid, not the vertically projected area. Storm volume is calculated using all levels occupied by the storm in the grid.

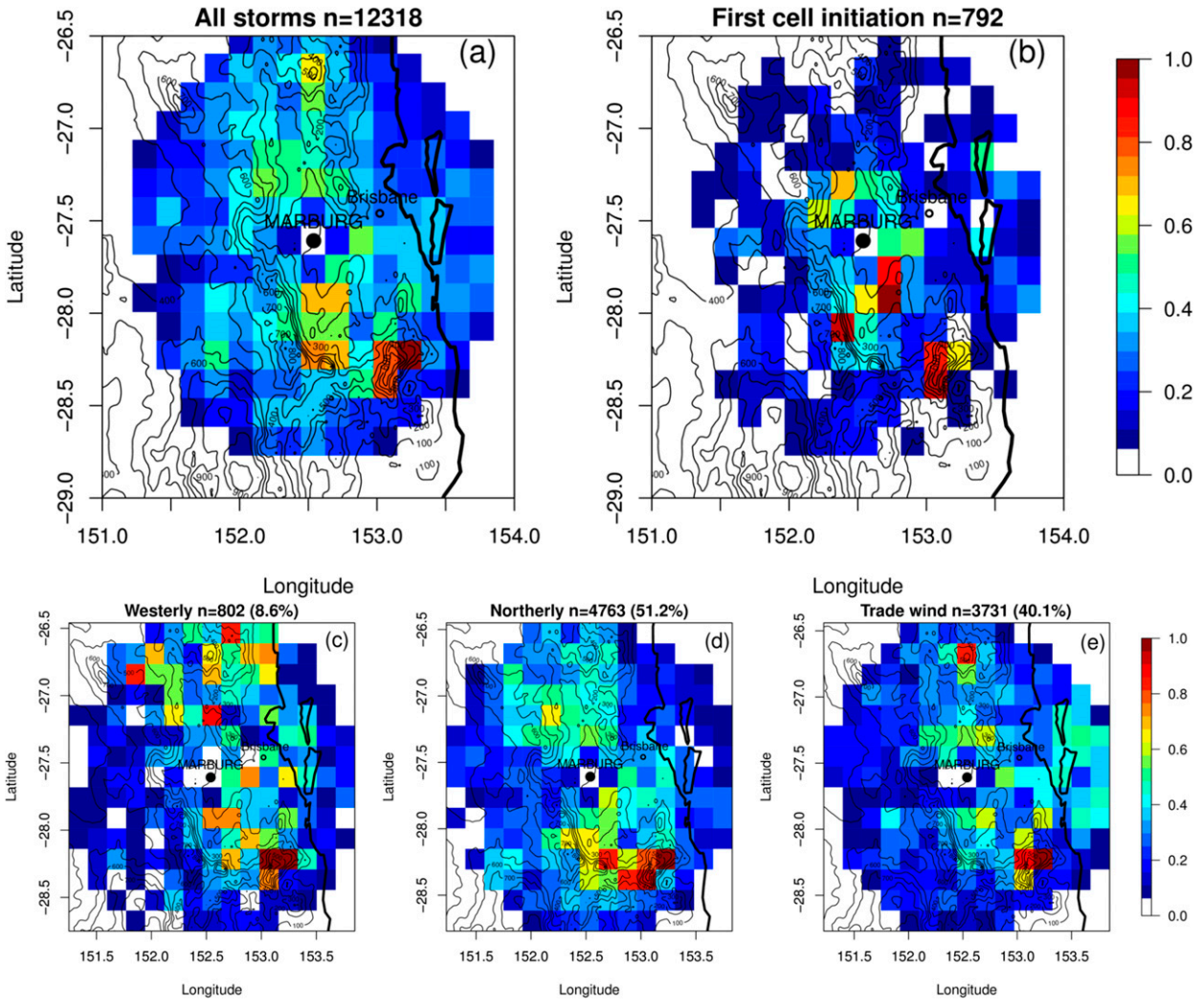

FIG. 6. Maps of spatial frequency of occurrence of storms observed by the Marburg radar for the period from April 2000 to July 2006. (a) Spatial frequency distribution for all storms in the range-restricted domain and (b) the spatial frequency of occurrence for the first TITAN track registered on a particular day. (c)–(e) The spatial frequency of occurrence for storm tracks for each of the synoptic regimes: westerly, northerly, and trade wind, respectively . The number of storms n measured in each regime is also indicated. The sum of the number of storms in each cluster (9296) is less than the total number of storms shown in (a) because not all days on which storms were registered in (a) were classified by the cluster analysis.

where the horizontal axis has been scaled logarithmically. The resulting histogram is nearly symmetrical, indicating that the convective precipitation area may be distributed lognormally. A visual degree of departure from normality can be determined from Fig. 8a. The horizontal axis is the precipitation area (on a logarithmic scale) and the vertical axis is the cumulative probability expected from a lognormal distribution with the same mean and standard deviation as the original data; the oblique line represents a perfect fit. The observed and the theoretical distributions coincide over several orders of magnitude of precipitation area through the range 15–200 km^2, which corresponds to a cumulative probability in the range 10%–95%. The extreme values of the observed distribution do not contain as many samples as predicted by a lognormal distribution. At smaller values of convective precipitation area the distribution has been truncated because of the condition of imposing a minimum volume of 30 km^3 for storm identification. Truncation of the distribution has also occurred at larger values of precipitation area because of physical and dynamical constraints placing an upper bound on precipitation area and also because of the possibility that some storms may penetrate the ''cone of silence'' and thus their size may be underestimated. Since the curves for all three regimes coincide, these observations

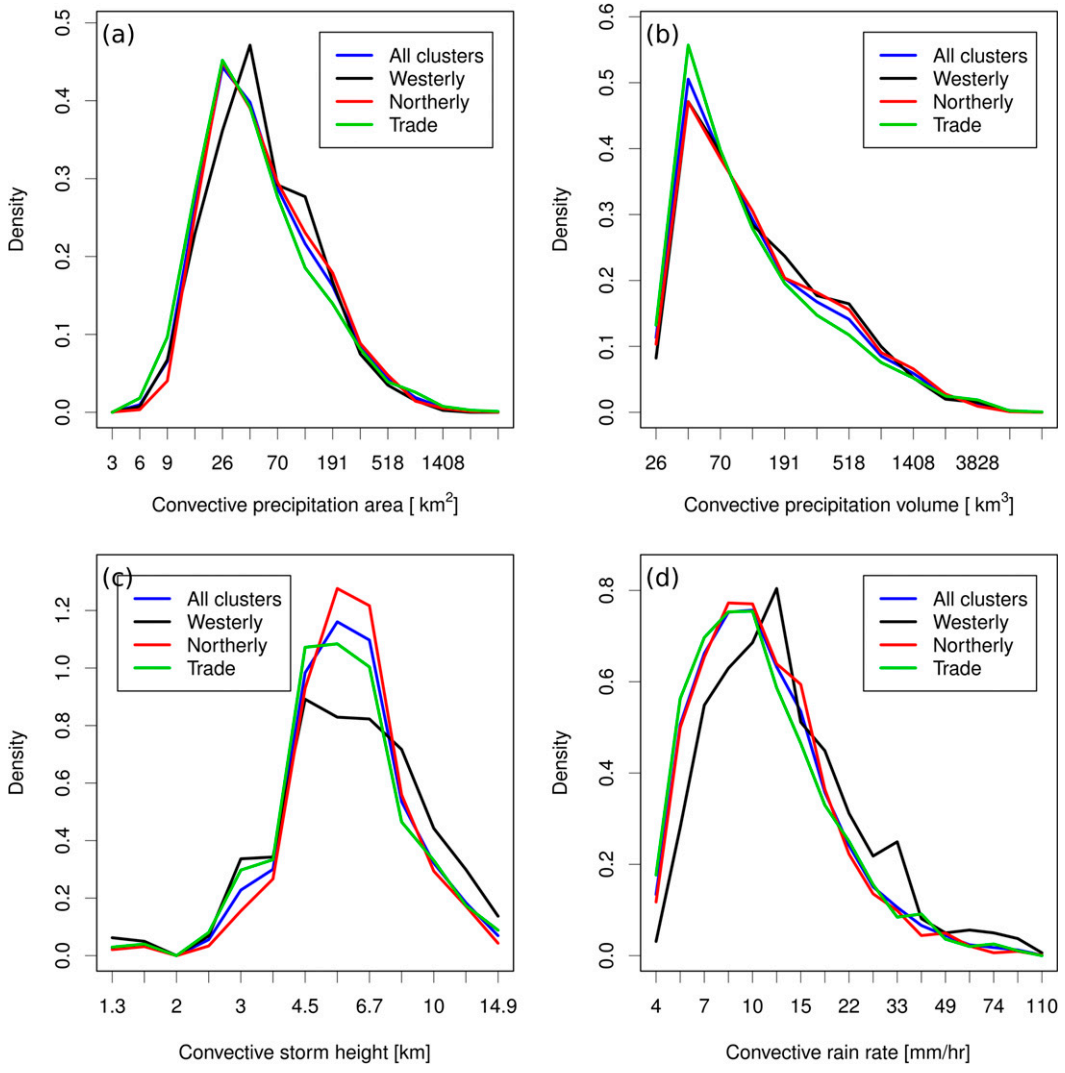

FIG. 7. Probability distribution functions of (a) precipitation area, (b) volume, (c) height, and (d) rain rate for convective storms. Curves are shown for the entire period and separately for each of the synoptic regimes.

indicate that a truncated lognormal distribution of convective precipitation area appears to be insensitive to the synoptic-scale forcing.

The areal coverage of precipitation in the westerly regime appears to be skewed to larger values than the other two regimes, especially the trade regime. To quantify whether this difference is statistically significant, the geometric mean and standard deviation were calculated and *t* tests performed on the log-transformed pdfs between each regime. The mean and standard deviation values are tabulated in Table 2, and means that are significantly different (at the 95% level) are denoted with an asterisk. The *t* test showed that the mean areal coverage of precipitation during the trade regime is statistically smaller than the westerly and northerly regimes; however, the difference between the northerly and westerly regimes was not significant. Therefore, despite storms in the westerly regime being skewed to larger sizes, on a climatological basis only the trade regime storms distinguish themselves by having a smaller mean areal coverage. The pdf and cumulative frequency of storm volume are shown in Figs. 7b and 8b, respectively. As for precipitation area, storm volume is also distributed lognormally. The geometric mean volume of the trade regime storms is the smallest and approximately 16 km^3 less than the westerly and northerly regimes, and this is reflected in the pdfs of Fig. 7b.

The pdf of convective storm-top height is shown in Fig. 7c and the cumulative frequency in Fig. 8c. Here, storm-top height is defined as the maximum height of the 35-dBZ echo achieved by a storm during each 10-min sample. For each regime, storm height is distributed

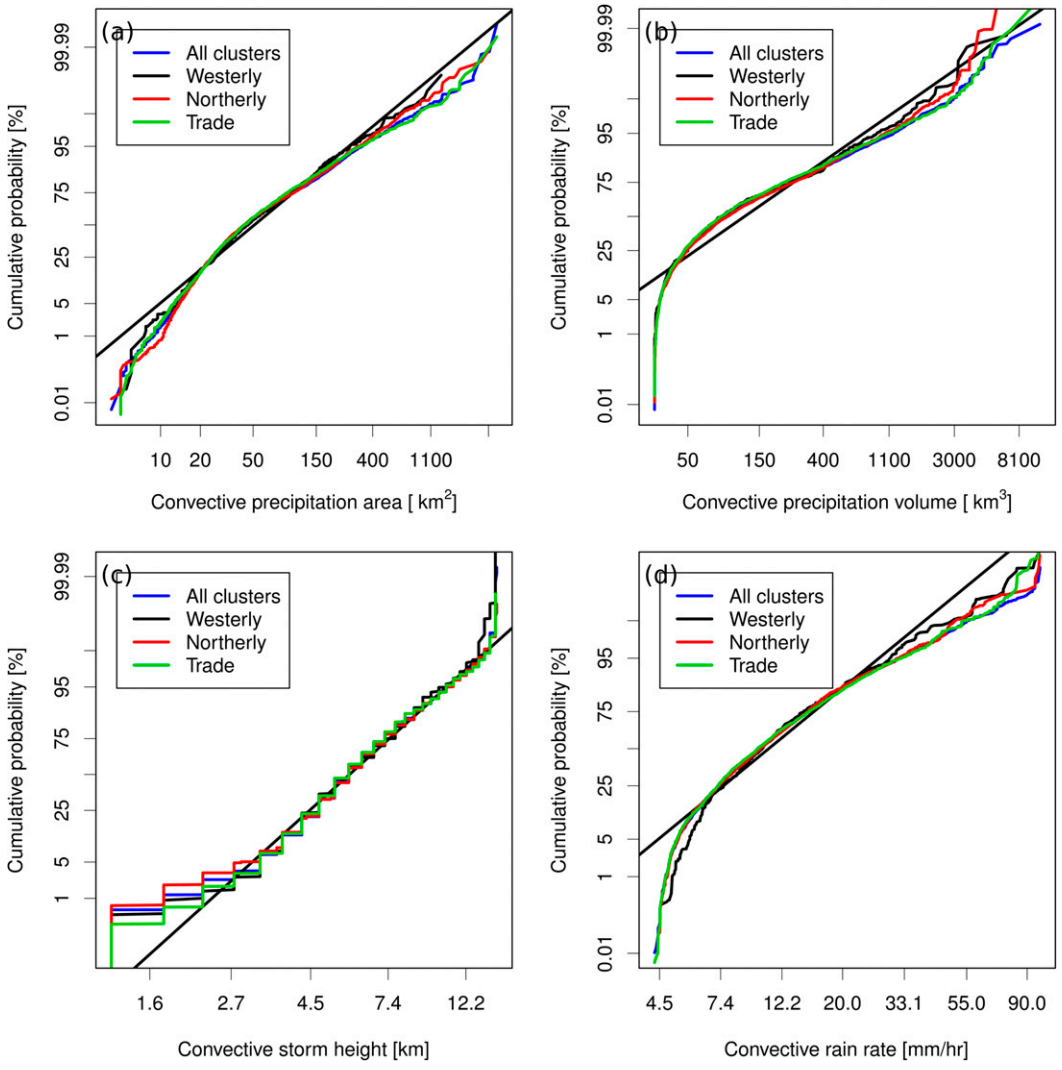

FIG. 8. Cumulative probability plots in log-probability format for each of the radar-derived variables shown in Fig. 7. The oblique black line represents the best-fit normal distribution to the all-clusters pdfs shown in Fig. 7.

lognormally throughout most of the troposphere, with significant departures occurring at the extremes. These departures occur for storms with heights below 3 km and above about 13 km, and can be interpreted with reference to the stability profiles of Fig. 5b. The departure near 13 km is caused by the inhibiting effect of the thermal tropopause, which restricts all but the most vigorous storms to below this height. At lower heights two modes are present in the pdf, one near 1.6 km and another near 3 km, and it is these that contribute to the departures from a lognormal distribution at heights below about 3 km.

From Fig. 5 it can be seen that the heights where these modes occur correspond to the climatological level of the trade inversion and the freezing level. This suggests that the presence of these stable layers increases the frequency of occurrence of convective storms with heights at these levels. However, the mode near the freezing level is pronounced for the trade and westerly regimes but absent for the northerly regime. The distinguishing feature of the stability profile of the westerly and trade regimes is the presence of a strong stable layer near the trade inversion, which is absent in the profile for the northerly regime. This suggests that the mode located near 3.5 km (in the westerly and trade regimes) forms because of the combined presence of the stable layer at the freezing level and the trade inversion below. Furthermore, despite the presence of an inversion near the freezing level in the northerly regime, the atmosphere is sufficiently unstable so as to (on average) allow convection to proceed through it.

Again, we conducted *t* tests to examine the statistical significance of the difference in the mean height of

TABLE 2. Storm-property summary statistics for the three synoptic clusters. The geometric mean is shown for variables that are distributed lognormally (area, volume, height, and rain rate), while the arithmetic mean is shown for the proportion of storm volume > 40 dBZ and storm lifetime. Values that are significantly different (at the 95% level) are marked with an asterisk.

	Synoptic cluster			
Storm property	All	Westerly	Northerly	Trade
Area (km^2)	51.1 ± 2.7	52.9 ± 2.6	53.8 ± 2.6	47.6 ± 2.8*
Vol (km^3)	119.6 ± 3.1	127.1 ± 3.0	126.2 ± 3.0	110.2 ± 3.0*
Top height (km)	5.8 ± 1.5	5.9 ± 1.6	5.9 ± 1.4	5.6 ± 1.5*
Rain rate (mm h^{-1})	11.0 ± 1.7	13.1 ± 1.8*	10.8 ± 1.7	10.7 ± 1.8
Vol > 40 dBZ (%)	21.0 ± 18.5	28.4 ± 29.6*	20.7 ± 17.9	19.9 ± 18.9
Speed (km h^{-1})	28.3 ± 17.5	33.4 ± 11.7*	29.4 ± 18.0	25.3 ± 17.0
Lifetime (min)	43.2 ± 4.2	38.7 ± 2.2	49.8 ± 6.2*	40.8 ± 5.3

storms between regimes. They indicated (see Table 2) that the mean height of trade wind storms is significantly less than in the other regimes. Additionally, northerly and westerly regime storms reach similar mean heights; however, the pdf (Fig. 7c) indicates westerly regime storms more often attain heights above 8 km. Despite the presence of modes near the trade and freezing-level inversions, the majority of storms in all regimes make it through these and into the midtroposphere, which results in storm-top height being well described by a continuous unimodal lognormal distribution between the freezing level and the tropopause. This span of heights is between 5% and 99% of the cumulative pdf. These observations hint as to the reason why some observations have indicated trimodal cloud-top-height distributions (e.g., Johnson et al. 1999), while others (e.g., May and Ballinger 2007) have observed a continuous distribution; it may be due to the stability profile of the atmosphere when the observations were obtained.

The pdf and accumulated frequency of precipitation rate are shown in Figs. 7d and 8d. The precipitation rate was derived from reflectivity using the relationship $Z = 500R^{1.3}$ and is the area-integrated rain rate of the lowest level of the TITAN-derived Cartesian grid. Since the Marburg radar is a single polarization radar, a reflectivity threshold for hail was set at 55 dBZ. Rain rate is distributed lognormally in the approximate range 5–30 mm h^{-1}, comprising about 85% of the cumulative total, with departures (indicative of a truncated lognormal distribution) only evident for light and extremely heavy rainfall events. The geometric mean rain rate for the westerly regime is the largest at 13 mm h^{-1}, about 2 mm h^{-1} larger than the other regimes. It can be seen from the pdf that the increased mean rain rate is due to a significant number of heavy rain events exceeding 20 mm h^{-1} and fewer moderate and light rain events (<10 mm h^{-1}). The heavier rain rate of westerly storms is associated with a larger fraction of the storms composed of reflectivities above 40 dBZ, as evidenced in Fig. 9.

c. *Comparison with other observations*

Table 3 compares the statistics of precipitation area and storm-top height with previous measurements obtained in a wide range of geographical locations; northwest Atlantic (Lopez 1976), eastern Atlantic (Houze and Cheng 1977), western Pacific (DeMott and Rutledge 1998), and Sydney (Potts et al. 2000). Our analysis has identified storms that are larger, both in areal extent and height, than those reported by Lopez (1976) and Houze and Cheng (1977). Those studies used the minimum detectable signal (as opposed to a 35-dBZ threshold) as criteria for identification of storm top. Using a smaller reflectivity threshold to define storm size one would expect, on average, to observe larger storms. However,

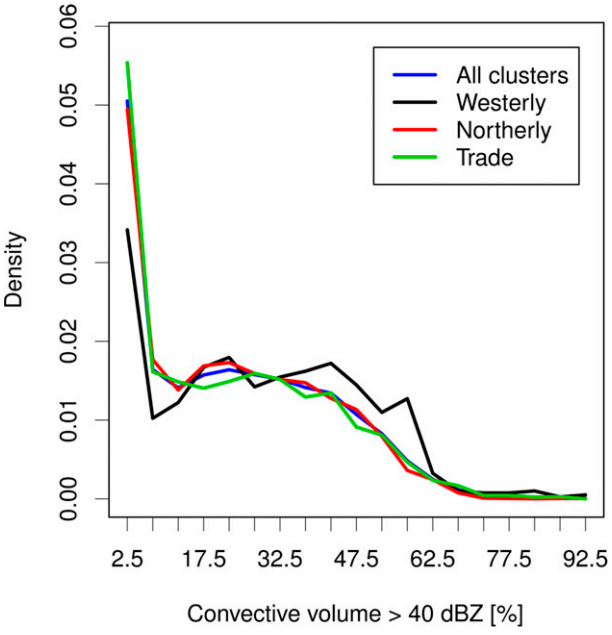

FIG. 9. Probability distribution function of the percentage of storm volume with a reflectivity > 40 dBZ.

TABLE 3. Comparison of the geometric mean of storm area and storm-top height from previous observations. The observations of (Lopez 1976) were obtained in the northwest Atlantic Ocean, those of (Houze and Cheng 1977) were obtained in the eastern Atlantic (during the GATE campaign), and those of (DeMott and Rutledge 1998) were obtained in the western Pacific during TOGA COARE.

Storm property	Author			
	Lopez	Houze and Cheng	DeMott and Rutledge	Potts
Area (km^2)	21	15	—	42
Top height (km)	4.5	4.1	5.4	5.3

the opposite is true, indicating that other factors are responsible for the observed larger storm sizes. The most likely candidate is due to the environment (either oceanic or continental) in which the storms formed. Potts et al. (2000) explained the origin of the larger storms observed in Sydney to the increased importance of ice phase processes in continental storms on the development of precipitation. Compared to the measurements of Potts et al. (2000) our observations show increases of approximately 10% and 20% in storm height and area. Sydney is about 900 km farther south than Brisbane and the tropopause height about 1 km (or 10%) lower suggesting the difference may be explained, in part, by the tropopause height.

A further comparison can be made by examining the contribution to areal coverage from differing size storms, which has been plotted in Fig. 10; similar results were published by Lopez (1976), Houze and Cheng (1977), and DeMott and Rutledge (1998), and we have included their measurements. The abscissa represents the cumulative frequency of echoes, ranked in increasing storm area, and the ordinate represents the cumulative areal coverage of convective precipitation. Curves are shown for each of the identified synoptic clusters, the complete dataset, and each of the aforementioned studies. It shows that, on average, the largest 20% of storms are responsible for about 67% of the areal coverage of convective precipitation. There is some variation among the clusters, so that the largest 20% of storms in the westerly cluster contribute just under 60% of the precipitation area, while the largest 20% in the trade cluster contribute about 70% of the precipitation area.

The curves for our results and previous observations exhibit some variability. As explained by Houze and Cheng (1977) and DeMott and Rutledge (1998), some of the difference can be attributed to radar sensitivity. The lower the sensitivity of a radar, the more likely it will distinguish high-reflectivity cores embedded in lower reflectivity as separate elements, while the higher-sensitivity

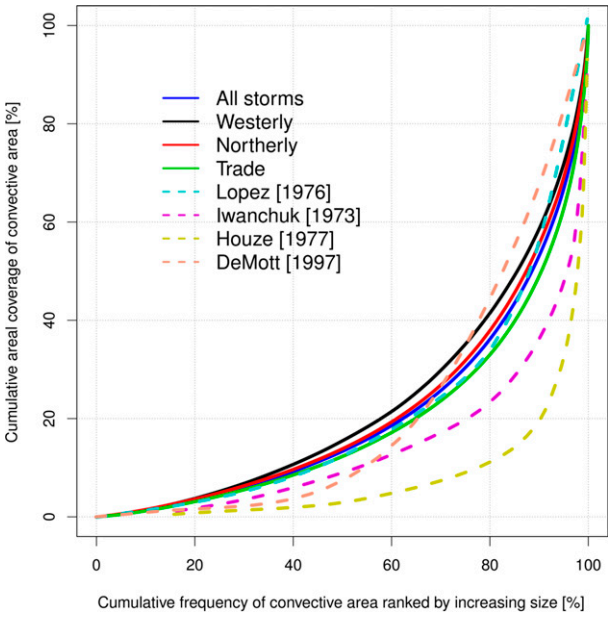

FIG. 10. Cumulative frequency distribution of fractional areal coverage of precipitation area. Curves are shown for all storms during the period 2000–06 and for the individual clusters. Results from previous experiments are also shown for comparison.

radar will measure it as a single element. As a result, measurements obtained with low-sensitivity radars [i.e., the results of Iwanchuk (1973) and Lopez (1976)] will measure a greater areal coverage of precipitation from smaller storms. Houze and Cheng (1977) explained the shift to the right of their curves compared to those of Iwanchuk (1973) and Lopez (1976) via the increased radar sensitivity in their study. However, the results of DeMott and Rutledge (1998), are comparable to those of Lopez (1976), despite using a higher-sensitivity radar. They attributed this to only considering convective elements as they first applied a convective–stratiform partitioning of the data using the method of Steiner et al. (1995). Our observations are similar to those of Lopez (1976) and DeMott and Rutledge (1998) so the differences between these results and those of Houze and Cheng (1977) are most likely due to only considering convective storms in our analysis. We cannot discount that the departure could be due to the different Cartesian grid resolution. Our study used 0.75 km in all dimensions, while that of DeMott and Rutledge (1998) used a 2-km resolution in the horizontal and a 0.5-km resolution in the vertical. Alternatively, since our observations were obtained over land with elevated topography and near the coast, the enhanced contribution of precipitation area from smaller storms may be a genuine reflection of the continental influence and/or convective enhancement from sea-breeze circulations.

d. Storm lifetime and exceedance times

Since TITAN distinguishes between storms that undergo mergers or splits and those that do not, the definition of storm lifetime can be ambiguous. Here we use the complex track number to determine storm lifetime thereby disregarding whether the storm had undergone a split or merger. The results are shown in Table 2. Since storm lifetime is not normally distributed, the appropriate test to apply to examine differences in the mean is the nonparametric Wilcoxon rank sum test (e.g., Wilks 2006). The westerly storms have the shortest mean lifetime, while the northerly regime storms have significantly longer (nearly 10 min) lifetimes. The longer mean storm lifetime of northerly storms is not surprising given they form in a less stable and moist environment than either trade or westerly storms. The complex storm-track lifetime cumulative distribution function is shown in Fig. 11. It shows that about 90% of westerly regime storms have a storm lifetime less than 45 min, compared with only about 80% and 70% of the trade and northerly regime storms. Therefore, the shorter mean lifetime of westerly and trade regime storms is mainly due to the preponderance of short-lived (lifetime less than 45 min) storms, which is likely due to the increased stability and lower humidity profiles of these regimes.

Figure 12 shows exceedance time plots for some of the aforementioned TITAN-derived variables. Each panel shows the percentage of time a variable exceeds a particular value, which was calculated as follows. First, a vector was constructed that spanned the range of values of a particular variable (e.g., precipitation area). The vector was then incremented and all values that exceeded the increment were identified. The exceedance time was then calculated as the total time of the storm entries scaled by the total for each regime separately. It therefore represents the percentage of time per day a variable exceeds a certain value for each regime.

It is worthwhile to consider the exceedance time plots in relation to the pdfs (Fig. 7) and Table 2. The analysis of storm size characteristics (area, volume, and height) demonstrated that storms in the trade wind regime are the smallest. In contrast, the exceedance times of storm area (not shown) and volume are consistently less for the westerly regime. Additionally, westerly regime storms have storm-top exceedance times less than those in the northerly regime and those of the trade regime for storms with tops below 8 km. The larger rain rates of westerly regime storms (see Fig. 7d) is evident in the exceedance times of precipitation rate and indirectly in the exceedance time curve of storm volume greater

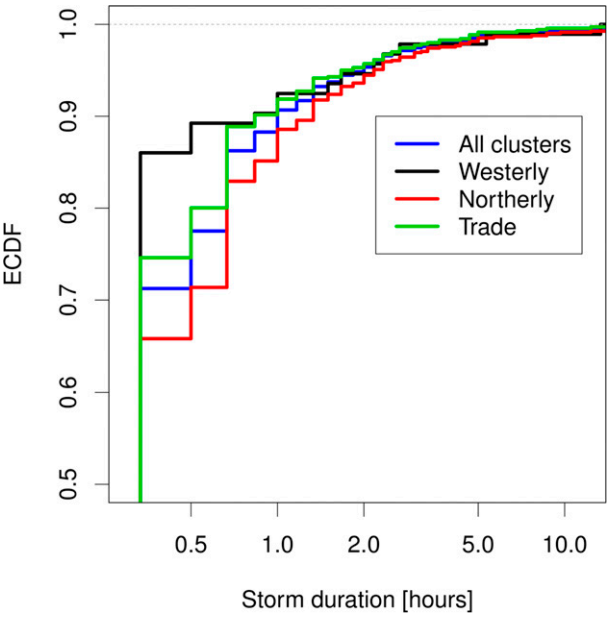

FIG. 11. Empirical cumulative distribution function of complex storm-track lifetime.

than 40 dBZ (Fig. 12d). It can be seen that westerly storms with exceptionally large convective rain rates have exceedance times comparable to those of storms in the northerly regime. Moreover, the exceedance times of westerly storms with a large fraction of high reflectivity are greater than in the other regimes.

When interpreted in light of the stability profiles presented in Fig. 5, an anticipated picture emerges: 1) the largest storms occur in the northerly regime since it is the most unstable and has the largest surface moisture and heat fluxes, and 2) the westerly regime produces relatively short-lived storms, most likely because of the very dry upper-level moisture profile that inhibits storm development. However, it is unexpected that rain rates in the westerly regime should be (on average) larger than the other, more unstable regimes. However, similar contrasts have been found in Darwin in tropical Australia where average rain rates during the "active" phase of the monsoon are generally higher than during the "break" period, although break period storms are generally larger and produce more lightning (Kumar et al. 2013b). Kumar et al. (2013b) attributed this to synoptic-scale forcing being responsible for storm activity during the active monsoon, while surface properties and mesoscale circulations become more important during the break period. Similarly, in SE Qld it appears that storms that form in the stable westerly flow are driven by large-scale forcing, while in the trade and northerly regimes the storms are driven by local heating and land–sea circulations.

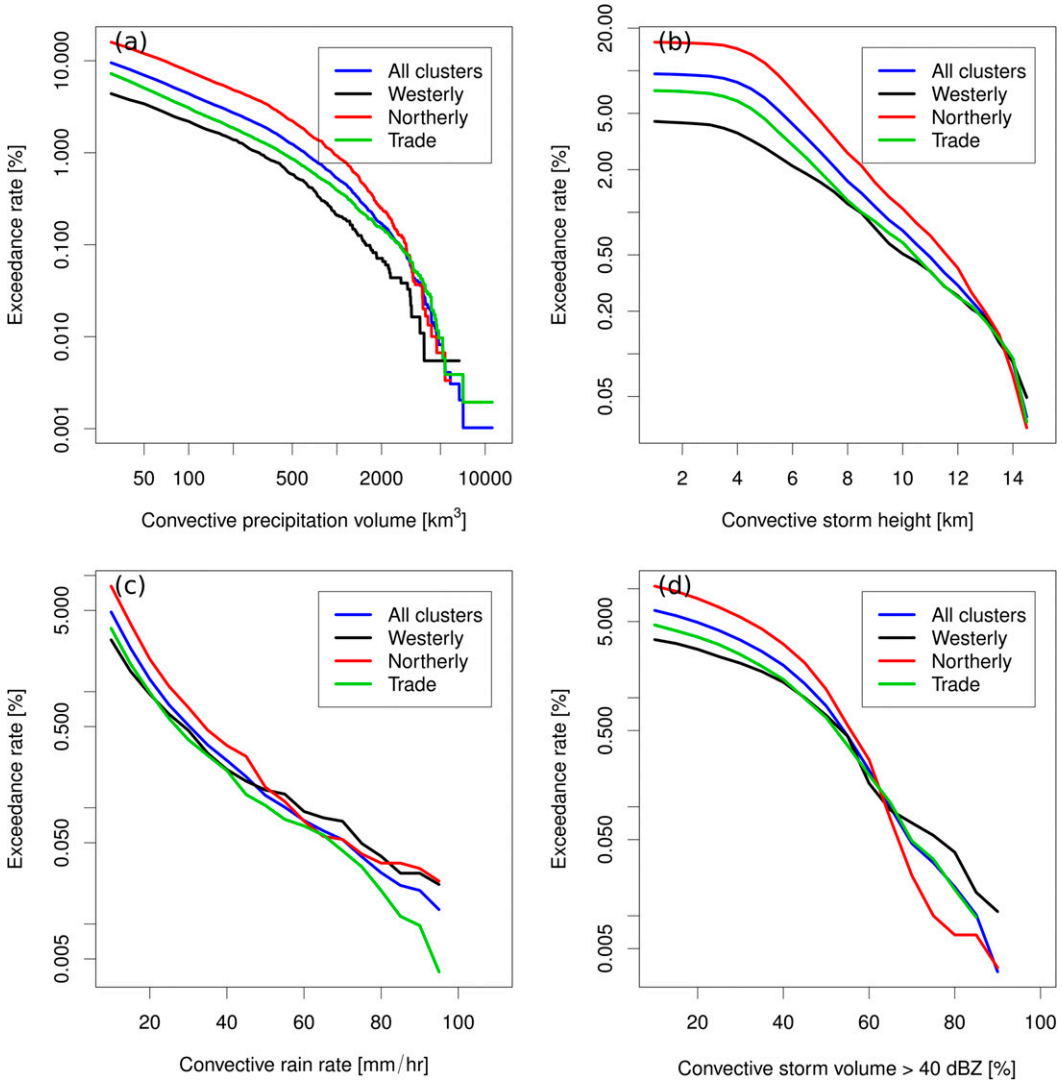

FIG. 12. Exceedance time plots of (a) precipitation volume, (b) height, and (c) rain rate, and (d) volume of storm with reflectivity > 40 dBZ for convective storms. The exceedance time has been expressed as a fraction of the total time for which storms were registered during a particular regime. Note that the ordinate (exceedance time expressed as a percentage) is on a logarithmic scale.

e. Storm motion

Probability distributions of storm speed and direction are shown in Figs. 13a and 13b, respectively, while the mean storm speed for each cluster is displayed in Table 2. Storms in the trade regime tend to move slowest, while those in the northerly and westerly regimes move faster. The pdfs of storm motion indicate storms in the trade regime have an increased propensity to move onshore, in line with the prevailing surface flow shown in Fig. 5, although their general propagation is from southwest to northeast. Likewise, northerly regime storms tend to move from the ranges toward the coast and offshore. The direction of propagation of storms is generally reflective of the range of climatological wind directions through the 850–700-hPa levels.

f. Temporal characteristics of precipitation

1) SEASONAL CYCLES

The convective precipitation area and rate as a function of month of year are shown in Figs. 14 and 15, respectively. Since the width of the boxes is proportional to the square root of the number of counts, it is apparent that they reflect the annual cycle of total water measured by the radiosondes (see Figs. 2 and 4). Furthermore, the seasonal cycle of total water is more highly correlated with the total rainfall recorded at Brisbane Airport (see Wilson

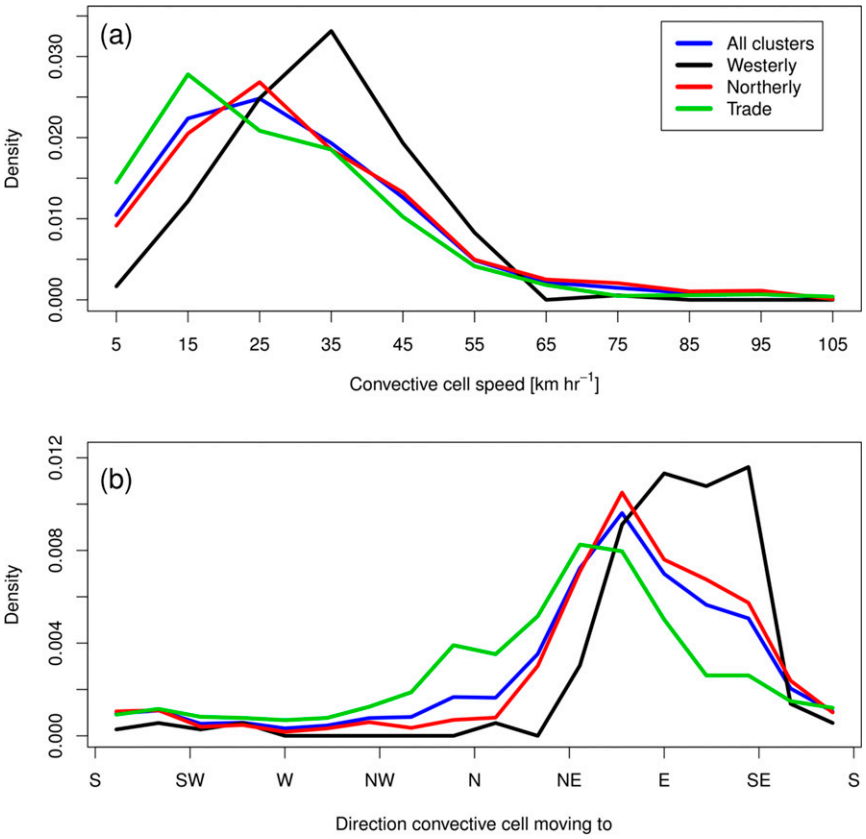

FIG. 13. Probability distributions of storm (a) speed and (b) direction.

et al. (2012) for a full description of the characteristics of Brisbane rainfall), than that of precipitation area and rate, indicating that total rainfall is determined foremost by the number of rainfall events, rather than their areal coverage or intensity. For instance, precipitation rate and area both have maxima during October, just before the peak rainfall months of November–March.

The seasonal cycle of the number of storms for the northerly and trade regimes also shows their propensity to occur mainly during the wet-season months (November–March). It reflects the seasonal cycle of the respective regime occurrence (see Fig. 4) and therefore their importance to rainfall contribution during this time. However, for the westerly regime, the number of recorded storms is more uniform throughout the year. This is in contrast to the seasonal cycle of westerly regime occurrence, which was mainly confined to winter and indicates that the probability of storms occurring in this regime is less subject to the wet–dry seasonal cycle.

2) DIURNAL CYCLES

The diurnal cycles of convective precipitation area and rate are shown in Figs. 16 and 17. The variables have been binned with respect to local Brisbane time (LT is UTC + 10 h). There is a strong signal that both parameters have an afternoon maximum and a weaker signal of an early morning maximum. The early morning peak in precipitation rate occurs around 0400 LT as does the precipitation area. However, the afternoon peak of rain rate occurs between 1400 and 1500 LT, while the peak in rain area occurs several hours later around 1800 LT. The lag is due to convective elements that detrain near the trade and freezing-level inversions (see Fig. 5) forming more widespread storms as the day progresses (e.g., Houze 1997).

The same signal occurs in the northerly and trade wind regimes, although the maximum in northerly regime rain rate is slightly later (1500 LT) than the 1400 LT maximum during the trade regime. Additionally, the maximum in rain rate during the trade regime drops off more rapidly than in the northerly regime indicating that northerly regime storms continue to precipitate heavily through the late evening. The diurnal cycle of westerly regime rain rate is less well defined, especially during the midmorning when the sample sizes are so small that the statistics are degraded. The fact that the mean statistics of storms in the trade and northerly regimes exhibit a strong diurnal cycle, coupled with the

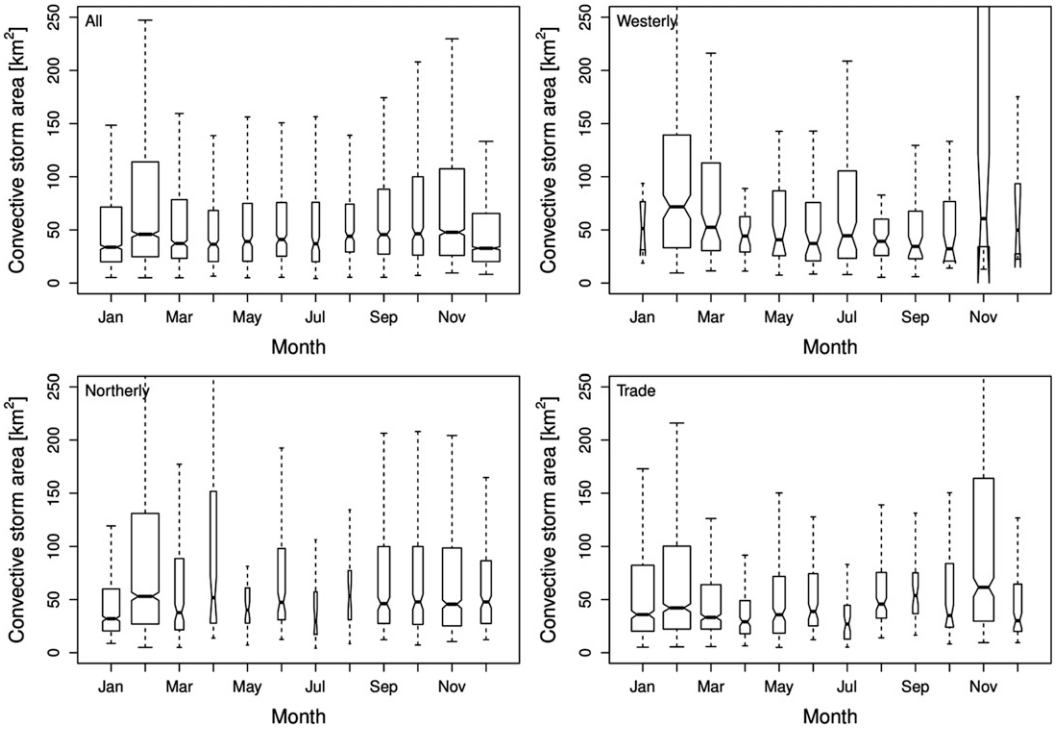

FIG. 14. Yearly cycle of convective storm area.

observation that most storms form just inland (see Fig. 6), is a strong indication that storm initiation in these regimes is dependent on surface heating and moisture, topographic uplift, and convergence along sea-breeze lines. These results are consistent with previous studies (e.g., Kumar et al. 2013b; Liu and Zipser 2008), which also found that continental convective onset was strongly determined by heating of the underlying surface and the sea breeze. The decreased amplitude of the diurnal cycle observed during the westerly regime further supports the observations of section 4d, which suggested that surface processes play less of a role in convective storms in this regime, but rather convective storms are driven by large-scale forcing.

The mechanism for the secondary peak in precipitation rate around 0400 LT is more complicated and has received less attention than that of the afternoon peak. However, Huang and Chan (2011), found a similar peak in early morning rainfall (as well as the main afternoon peak) in southeast China, which they attributed to the semidiurnal flux of water vapor from ocean to land. More investigations are needed to determine if similar mechanisms are responsible here.

5. Summary and conclusions

Upper-air radiosonde data obtained over seven years (January 2001–March 2008) and S-band weather radar data over a six-year period (January 2001–December 2006) were synthesized to investigate the statistics of convective storm systems near Brisbane in southeast Queensland. Dynamic and thermodynamic variables (wind direction and shear, static stability, moisture flux, and total integrated water) were derived from the radiosonde data and used as input to a *K*-means clustering algorithm to objectively identify synoptic regimes of the SE Qld region. Three distinct synoptic regimes were identified, distinguished primarily by moisture and stability fields. The regimes were classified as 1) a dry, stable regime with mainly westerly winds; 2) a moist, unstable regime with northerly winds; and 3) a moist, unstable regime with southeasterly winds. These were labeled as westerly, northerly, and trade regimes, respectively. The northerly and trade regimes occurred primarily during the summer months (November–March), while the westerly regime mainly occurred during winter (April–October). A total of 2541 soundings were used for the cluster analysis and the relative contribution to each cluster was 26% (659), 26% (658), and 48% (1224) for the westerly, northerly, and trade wind regimes, respectively. These figures, however, included days in which no convective storms were observed by the radar. When storms were observed, which occurred on 932 individual days, the proportions became 20% (189), 29% (267), and 51% (476).

The radar measurements were obtained from the Bureau of Meteorology's Marburg radar, situated approximately 55 km southwest of Brisbane Airport, and were

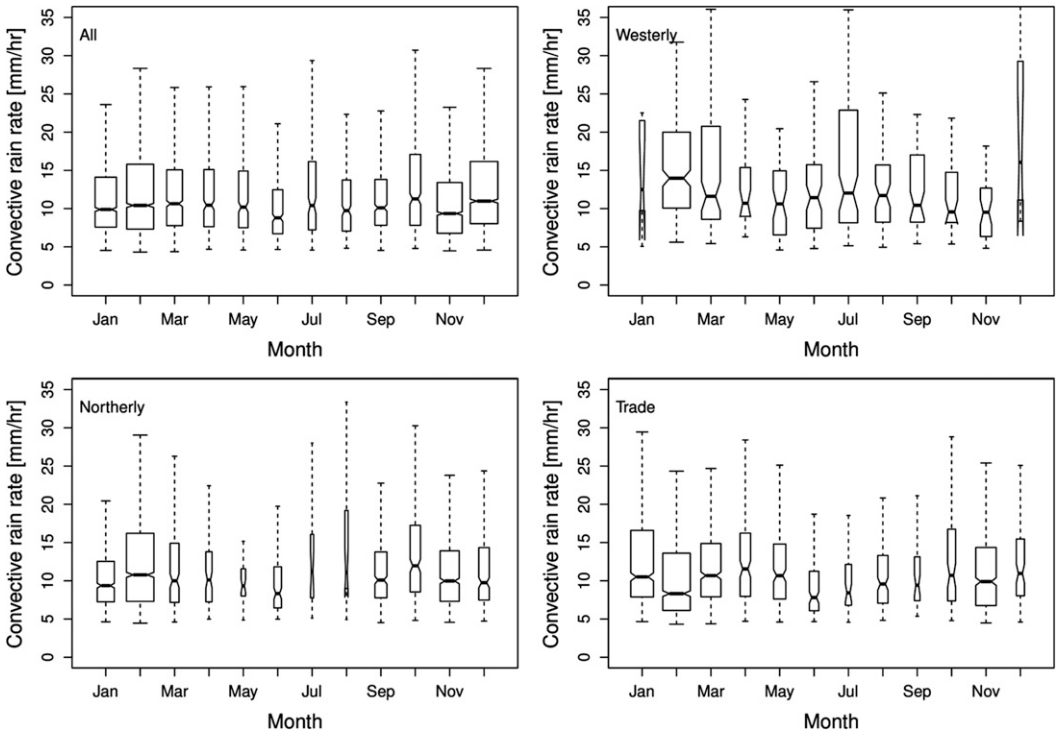

FIG. 15. As in Fig. 14, but for convective rain rate.

used to calculate storm statistics. An objective method of storm identification and classification [Thunderstorm Identification, Tracking, Analysis, and Nowcasting (TITAN)] was applied to the radar observations and various statistics of the storms analyzed. The minimum volume and reflectivity threshold specified to define a storm were 30 km^3 and 35 dBZ, respectively. The storm statistics examined included initiation location, storm area and volume, convective rain rate, and storm-top height (specified by the 35-dBZ reflectivity threshold), the volume of a cell greater than 40 dBZ and storm speed and direction. Yearly and diurnal cycles of precipitation area and rate were also evaluated. Furthermore, the statistics were evaluated for storms during the entire period and for the separate synoptic regimes determined from the cluster analysis. The main findings of this study are as follows:

- There was an increase in frequency of convective storm location and initiation along the mountain ranges when compared with the coastal regions. This was true when the synoptic regimes were considered individually or as a whole.
- Storm area, volume, height, and rain rate were well described by truncated lognormal distributions. The same result was found when each of the synoptic regimes were considered individually, suggesting the lognormal fit is insensitive to the synoptic forcing.
- There were differences in the mean and standard deviation of the above variables among the regimes and Student's t tests were applied to examine if the differences were statistically significant. It was found that trade wind regime storms were the smallest by all measures of size and that westerly regime storms had the largest rain rates.
- The results were compared with similar statistics obtained during the GATE and TOGA COARE experiments and measurements made in Sydney. The convective storms measured in SE Qld were found to have sizes more typical of continental storms although slightly larger and taller than those measured in Sydney. Consistent with other studies it was found that about the largest 10% of storms were responsible for about 50% of convective areal coverage. However, it was found that small storms contribute more to precipitation coverage than in oceanic regions, which was ascribed to topographic and land–sea interactions enhancing precipitation.
- Some evidence of trimodal storm-top heights was found with modes located near the climatological trade inversion (1.5–2 km) and freezing level (3.5–4 km). However, the presence of all three modes was only observed for the westerly and trade regimes as the freezing level mode was absent for northerly regime storms. The distinguishing feature of the thermodynamic profile of the westerly and trade regimes was the presence of a stable inversion located near

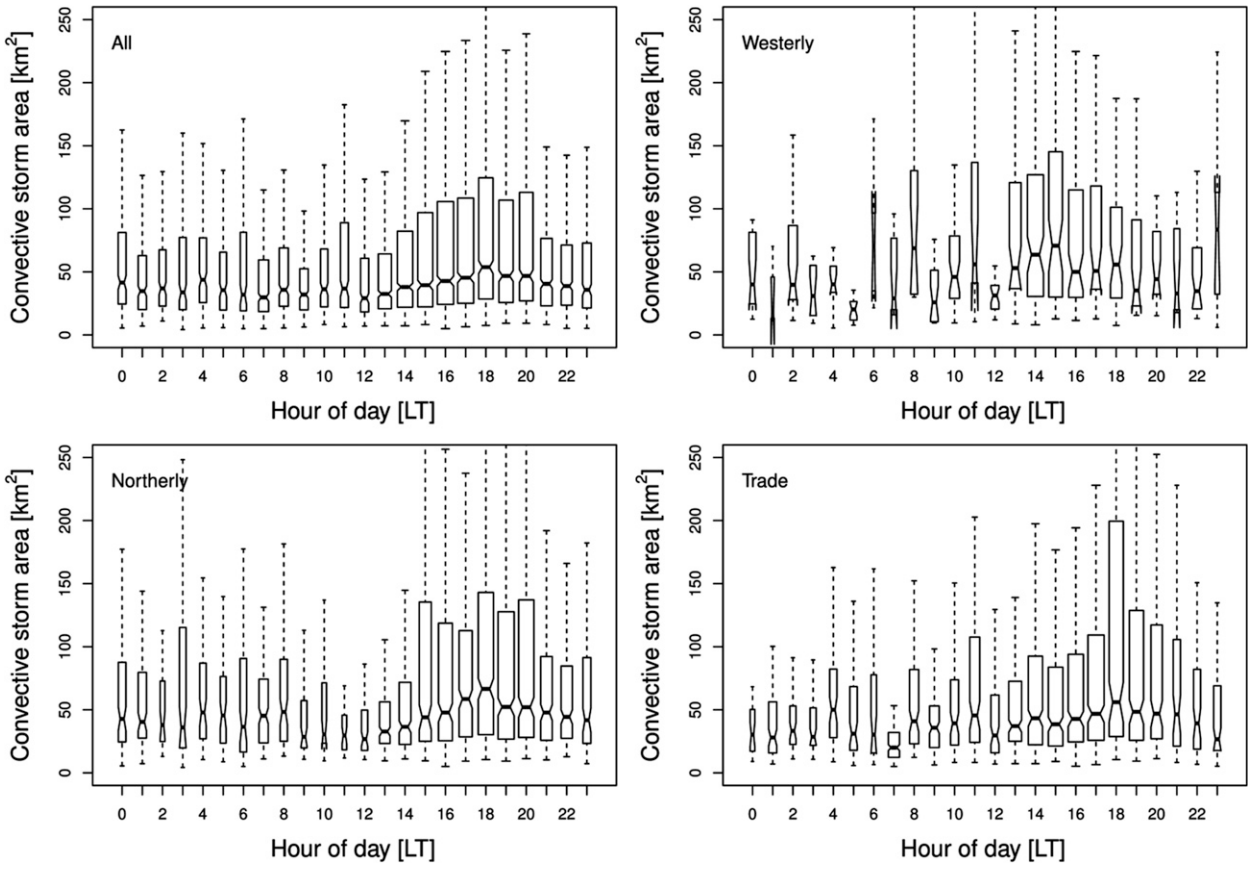

FIG. 16. Diurnal cycle of convective storm area.

1.5–2 km that was absent in the northerly regime thermodynamic profile. This suggested that a storm-top-height mode near the freezing level is more likely to occur if a low-level trade inversion is also present.

- Storms in the westerly regime had the shortest mean lifetime, which was due to many very short lifetime (less than 30 min) storms being present. The shorter lifetime of these storms was attributed to the very dry humidity profiles observed. This was contrasted with exceedance time plots that indicated that, despite westerly regime storms having the shortest lifetimes, they generally have larger rain rates.
- Westerly regime storms had the largest average storm speed, although northerly and trade regime storms had the largest absolute speeds. Storms in the northerly and westerly regimes tend to propagate from west to east (i.e., from inland to offshore), while those of the trade regime had an increased tendency to move inland from the ocean.
- The convective precipitation area and rain rate reflected the annual cycle of radiosonde-derived total water, that is, increases during the wet season and decreases during the dry season. This cycle was especially evident in the northerly and trade regimes. In contrast, the seasonal cycle of precipitation area and rate was less defined for storms in the westerly regime, such that there was no preferred time of year for their occurrence.
- The diurnal cycle of rain rate and convective precipitation area exhibited a major midafternoon maximum and a secondary early morning peak. The same signal was observed for storms in the trade and northerly regimes. Moreover, the peak in precipitation area lagged that of rain rate by several hours, which was interpreted as isolated convective precipitation transitioning to a more widespread event as the day progressed. The early morning peak in rain rate was absent for the westerly regime, and the afternoon peak was less defined, further supporting that convective storms in this regime are driven by large-scale forcing and less influenced by surface properties and land–sea breezes.

The main value of this study has been to provide a broad overview of the properties of convective storms in SE Qld using historical volumetric radar data and to understand how these properties change under objectively

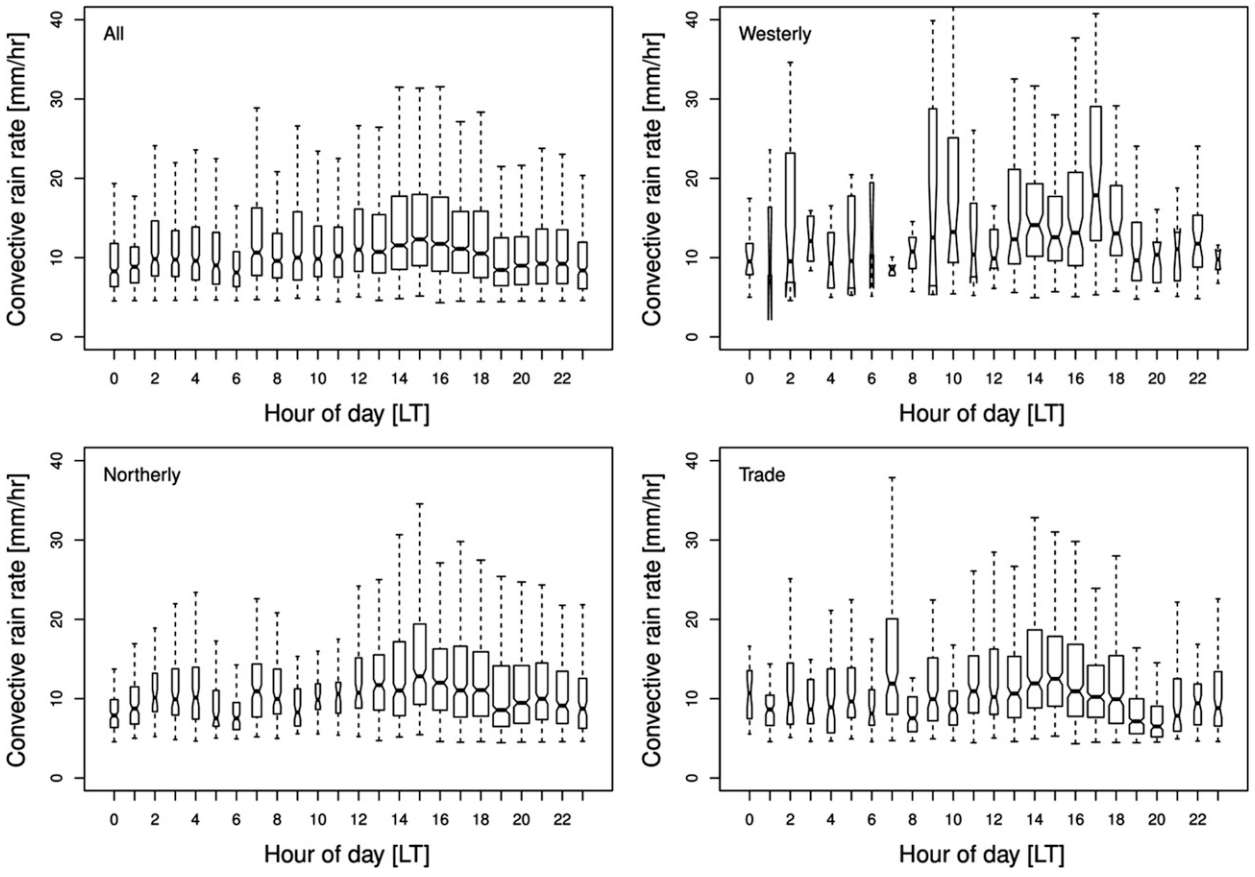

FIG. 17. As in Fig. 16, but for convective rain rate.

defined synoptic conditions. This work employed observations from one radar (Marburg), covering the period January 2001 to December 2006, which was an exceptionally dry period in SE Qld. The region has since experienced several years of above average rainfall and floods, especially during 2011 when a La Niña occurred, so it would be worthwhile to extend the study period. Additionally, a second more modern radar with Doppler capabilities and located closer to the coast (Mount Stapylton) was added to the Bureau's operational radar network in 2007. Observations from this radar will enable us to independently compare the convective storm properties and to identify if problems associated with the data quality control have adversely affected these results. Since the Mount Stapylton radar is located at the coast it will also allow better observations of the contrasts between oceanic and continental convective storms and the influence of sea-breeze circulations on their formation. Furthermore, a dual-polarimetric research radar (CP2) located midway between the Marburg and Mount Stapylton radars has obtained some limited observations that we plan to use to examine microphysical differences between storms in the different regimes. Finally, there have been some recent additions to the TITAN software, whereby the Steiner et al. (1995) convective–stratiform partitioning can be performed and storm identification constrained to the convective regions. Initial tests suggest that the subsequent TITAN-identified storms are substantially smaller when the partitioning is performed. We plan to investigate how this will affect the statistics presented here.

Acknowledgments. The authors thank four anonymous reviewers for their thorough and constructive comments that have significantly improved the structure and content of the manuscript. We also thank Robert Wilson of the Australian Bureau of Meteorology for providing the Marburg radar dataset and Mike Dixon from the National Center for Atmospheric Research for useful discussions regarding the TITAN storm analysis software. Doctors Alain Protat and Vickal Kumar contributed many useful comments and constructive criticism that helped guide this work at its later stages. The contribution of Scott Collis through Argonne National Laboratory was supported by the U.S. Department of Energy, Office of Science, Office of Biological and Environmental

Research, under Contract DE-AC02-06CH11357. This research was primarily supported by The Queensland Government Department of Environment and Resource Management through the Queensland Climate Change Centre of Excellence.

REFERENCES

Abbs, D., and K. McKinnes, 2004: Analysis of extreme rainfall and wind events in a GCM. The impact of climate change in extreme rainfall and coastal sea levels over south-east Queensland, Part 1, CSIRO, 48 pp. [Available online at http://www.hpsc.csiro.au/users/69999/TCs_extreme_rainfall_reports/gccc_report_final_200411.doc.]

Bellon, A., and I. Zawadzki, 2003: A 9-year summary of radar characteristics of mesocyclonic storms and of deep convection in southern Quebec. *Atmos.–Ocean*, **41**, 99–120, doi:10.3137/ao.410201.

Browning, K. A., and Coauthors, 2007: The Convective Storm Initiation Project. *Bull. Amer. Meteor. Soc.*, **88**, 1939–1955, doi:10.1175/BAMS-88-12-1939.

Cahalan, R., and J. Joseph, 1989: Fractal statistics of cloud fields. *Mon. Wea. Rev.*, **117**, 261–272, doi:10.1175/1520-0493(1989)117<0261:FSOCF>2.0.CO;2.

Carbone, R. E., J. D. Tuttle, D. A. Ahijevych, and S. B. Trier, 2002: Inferences of predictability associated with warm season precipitation episodes. *J. Atmos. Sci.*, **59**, 2033–2056, doi:10.1175/1520-0469(2002)059<2033:IOPAWW>2.0.CO;2.

Cetrone, J., and R. Houze, 2006: Characteristics of tropical convection over the ocean near Kwajalein. *Mon. Wea. Rev.*, **134**, 834–853, doi:10.1175/MWR3075.1.

Chen, M., Y. Wang, F. Gao, and X. Xiao, 2012: Diurnal variations in convective storm activity over contiguous North China during the warm season based on radar mosaic climatology. *J. Geophys. Res.*, **117**, D20115, doi:10.1029/2012JD018158.

——, ——, ——, and ——, 2014: Diurnal evolution and distribution of warm-season convective storms in different prevailing wind regimes over contiguous north China. *J. Geophys. Res. Atmos.*, **119**, 2742–2763, doi:10.1002/2013JD021145.

Cheng, C., and R. Houze, 1979: The distribution of convective and mesoscale precipitation in GATE radar echo patterns. *Mon. Wea. Rev.*, **107**, 1370–1381, doi:10.1175/1520-0493(1979)107<1370:TDOCAM>2.0.CO;2.

Cifelli, R., S. W. Nesbitt, S. A. Rutledge, W. A. Petersen, and S. Yuter, 2007: Radar characteristics of precipitation features in the EPIC and TEPPS regions of the east Pacific. *Mon. Wea. Rev.*, **135**, 1576–1595, doi:10.1175/MWR3340.1.

Collis, S., A. Protat, and K. Chung, 2010: The effect of radial velocity gridding artifacts on variationally retrieved vertical velocities. *J. Atmos. Oceanic Technol.*, **27**, 1239–1246, doi:10.1175/2010JTECHA1402.1.

Connor, G., and M. Bonnel, 1998: Air mass and dynamic parameters affecting trade wind precipitation on the northeast Queensland tropical coast. *Int. J. Climatol.*, **18**, 1357–1372, doi:10.1002/(SICI)1097-0088(1998100)18:12<1357::AID-JOC317>3.0.CO;2-Z.

DeMott, C. A., and S. A. Rutledge, 1998: The vertical structure of TOGA COARE convection. Part I: Radar echo distributions. *J. Atmos. Sci.*, **55**, 2730–2747, doi:10.1175/1520-0469(1998)055<2730:TVSOTC>2.0.CO;2.

Dixon, M., and G. Weiner, 1993: TITAN: Thunderstorm Identification, Tracking, Analysis, and Nowcasting—A radar-based methodology. *J. Atmos. Oceanic Technol.*, **10**, 785–797, doi:10.1175/1520-0426(1993)010<0785:TTITAA>2.0.CO;2.

Gong, X., and M. Richman, 1995: On the application of cluster analysis to growing season precipitation data in North America east of the Rockies. *J. Climate*, **8**, 897–931, doi:10.1175/1520-0442(1995)008<0897:OTAOCA>2.0.CO;2.

Goudenhoofdt, E., and L. Delobbe, 2013: Statistical characteristics of convective storms in Belgium derived from volumetric weather radar observations. *J. Appl. Meteor. Climatol.*, **52**, 918–934, doi:10.1175/JAMC-D-12-079.1.

Hartigan, J., and M. Wong, 1979: A *K*-means clustering algorithm. *Appl. Stat.*, **28**, 100–108, doi:10.2307/2346830.

Haynes, J. M., and G. L. Stephens, 2007: Tropical oceanic cloudiness and the incidence of precipitation: Early results from CloudSat. *Geophys. Res. Lett.*, **34**, L09811, doi:10.1029/2007GL029335.

Hopkins, L., and G. Holland, 1997: Australian heavy-rain days and associated east coast cyclones: 1958–92. *J. Climate*, **10**, 621–635, doi:10.1175/1520-0442(1997)010<0621:AHRDAA>2.0.CO;2.

Houze, R. A., 1997: Stratiform precipitation in regions of convection: A meteorological paradox? *Bull. Amer. Meteor. Soc.*, **78**, 2179–2196, doi:10.1175/1520-0477(1997)078<2179:SPIROC>2.0.CO;2.

——, and C.-P. Cheng, 1977: Radar characteristics of tropical convection observed during GATE: Mean properties and trends over the summer season. *Mon. Wea. Rev.*, **105**, 964–980, doi:10.1175/1520-0493(1977)105<0964:RCOTCO>2.0.CO;2.

Huang, W.-R., and J. C. L. Chan, 2011: Maintenance mechanisms for the early-morning maximum summer rainfall over southeast China. *Quart. J. Roy. Meteor. Soc.*, **137**, 959–968, doi:10.1002/qj.815.

Iwanchuk, R., 1973: Characteristics and distribution of precipitation areas over the tropical Atlantic. M.S. thesis, Dept. of Meteorology, Massachusetts Institute of Technology, 106 pp.

Johnson, R. H., P. E. Ciesielski, and K. A. Hart, 1996: Tropical inversions near the 0°C level. *J. Atmos. Sci.*, **53**, 1838–1855, doi:10.1175/1520-0469(1996)053<1838:TINTL>2.0.CO;2.

——, T. M. Rickenbach, S. A. Rutledge, P. E. Ciesielski, and W. H. Schubert, 1999: Trimodal characteristics of tropical convection. *J. Climate*, **12**, 2397–2418, doi:10.1175/1520-0442(1999)012<2397:TCOTC>2.0.CO;2.

Keenan, T. D., and R. E. Carbone, 2008: Propagation and diurnal evolution of warm season cloudiness in the Australian and Maritime Continent region. *Mon. Wea. Rev.*, **136**, 973–994, doi:10.1175/2007MWR2152.1.

Klingaman, N. P., 2012: A literature survey of key rainfall drivers in Queensland, Australia: Rainfall variability and change. Rainfall in Queensland, Part 1, Office of Climate Change, QCCCE Research Rep., 37 pp. [Available online at https://www.longpaddock.qld.gov.au/about/publications/pdf/walker-report-part-1.pdf.]

Kumar, V. V., C. Jakob, A. Protat, P. T. May, and L. Davies, 2013a: The four cumulus cloud modes and their progression during rainfall events: A C-band polarimetric radar perspective. *J. Geophys. Res. Atmos.*, **118**, 8375–8389, doi:10.1002/jgrd.50640.

——, A. Protat, P. T. May, C. Jakob, G. Penide, S. Kumar, and L. Davies, 2013b: On the effects of large-scale environment and surface types on convective cloud characteristics over Darwin, Australia. *Mon. Wea. Rev.*, **141**, 1358–1374, doi:10.1175/MWR-D-12-00160.1.

Lang, T. J., D. A. Ahijevych, S. W. Nesbitt, R. E. Carbone, and S. A. Rutledge, 2007: Radar-observed characteristics of precipitating

systems during NAME 2004. *J. Climate*, **20**, 1713–1733, doi:10.1175/JCLI4082.1.

Li, J., R. Yu, and T. Zhou, 2008: Seasonal variation of the diurnal cycle of rainfall in southern contiguous China. *J. Climate*, **21**, 6036–6043, doi:10.1175/2008JCLI2188.1.

Liu, C., and E. J. Zipser, 2008: Diurnal cycles of precipitation, clouds, and lightning in the tropics from 9 years of TRMM observations. *Geophys. Res. Lett.*, **35**, L04819, doi:10.1029/2007GL032437.

Lopez, R., 1976: Radar characteristics of the cloud population of tropical disturbances in the northwest Atlantic. *Mon. Wea. Rev.*, **104**, 268–283, doi:10.1175/1520-0493(1976)104<0268:RCOTCP>2.0.CO;2.

——, 1977: The lognormal distribution and cumulus cloud populations. *Mon. Wea. Rev.*, **105**, 865–872, doi:10.1175/1520-0493(1977)105<0865:TLDACC>2.0.CO;2.

Lucas, C., and E. Zipser, 2000: Environmental variability during TOGA COARE. *J. Atmos. Sci.*, **57**, 2333–2350, doi:10.1175/1520-0469(2000)057<2333:EVDTC>2.0.CO;2.

Malkus, J. S., and H. Riehl, 1964: Cloud structure and distributions over the tropical Pacific Ocean. *Tellus*, **16**, 275–287, doi:10.1111/j.2153-3490.1964.tb00167.x.

Matthews, C., and B. Geerts, 1995: Characteristic thunderstorm distribution in the Sydney area. *Aust. Meteor. Mag.*, **44**, 127–138.

May, P. T., and A. Ballinger, 2007: The statistical characteristics of convective cells in a monsoon regime (Darwin, northern Australia). *Mon. Wea. Rev.*, **135**, 82–92, doi:10.1175/MWR3273.1.

——, J. H. Mather, G. Vaughan, K. N. Bower, C. Jakob, G. M. McFarquhar, and G. G. Mace, 2008: The Tropical Warm Pool International Cloud Experiment. *Bull. Amer. Meteor. Soc.*, **89**, 629–645, doi:10.1175/BAMS-89-5-629.

——, C. N. Long, and A. Protat, 2012: The diurnal cycle of the boundary layer, convection, clouds, and surface radiation in a coastal monsoon environment (Darwin, Australia). *J. Climate*, **25**, 5309–5326, doi:10.1175/JCLI-D-11-00538.1.

Neggers, R., H. Jonker, and A. Siebesma, 2003: Size statistics of cumulus cloud populations in large-eddy simulations. *J. Atmos. Sci.*, **60**, 1060–1074, doi:10.1175/1520-0469(2003)60<1060:SSOCCP>2.0.CO;2.

Nesbitt, S. W., and E. J. Zipser, 2003: The diurnal cycle of rainfall and convective intensity according to three years of TRMM measurements. *J. Climate*, **16**, 1456–1475, doi:10.1175/1520-0442-16.10.1456.

Noda, A. T., K. Oouchi, M. Satoh, and H. Tomita, 2012: Quantitative assessment of diurnal variation of tropical convection simulated by a global nonhydrostatic model without cumulus parameterization. *J. Climate*, **25**, 5119–5134, doi:10.1175/JCLI-D-11-00295.1.

Pope, M., C. Jakob, and M. Reeder, 2009a: Objective classification of tropical mesoscale convective systems. *J. Climate*, **22**, 5797–5805, doi:10.1175/2009JCLI2777.1.

——, ——, and ——, 2009b: Regimes of the north Australian wet season. *J. Climate*, **22**, 6699–6715, doi:10.1175/2009JCLI3057.1.

Potts, R., T. Keenan, and P. May, 2000: Radar characteristics of storms in the Sydney area. *Mon. Wea. Rev.*, **128**, 3308–3319, doi:10.1175/1520-0493(2000)128<3308:RCOSIT>2.0.CO;2.

Saxen, T. R., and Coauthors, 2008: The operational mesogamma-scale analysis and forecast system of the U.S. Army Test and Evaluation Command. Part IV: The White Sands Missile-Range Auto-Nowcast system. *J. Appl. Meteor. Climatol.*, **47**, 1123–1139, doi:10.1175/2007JAMC1656.1.

Steiner, M., R. A. Houze Jr., and S. Yuter, 1995: Climatological characterization of three-dimensional storm structure from operational radar and rain gauge data. *J. Appl. Meteor.*, **34**, 1978–2007, doi:10.1175/1520-0450(1995)034<1978:CCOTDS>2.0.CO;2.

Sun, J., and Coauthors, 2014: Use of NWP for nowcasting convective precipitation: Recent progress and challenges. *Bull. Amer. Meteor. Soc.*, **95**, 409–426, doi:10.1175/BAMS-D-11-00263.1.

Tessendorf, S. A., and Coauthors, 2012: The Queensland Cloud Seeding Research Program. *Bull. Amer. Meteor. Soc.*, **93**, 75–90, doi:10.1175/BAMS-D-11-00060.1.

Tudurí, E., and C. Ramis, 1997: The environments of significant convective events in the western Mediterranean. *Wea. Forecasting*, **12**, 294–306, doi:10.1175/1520-0434(1997)012<0294:TEOSCE>2.0.CO;2.

Weckwerth, T. M., and Coauthors, 2004: An overview of the International H_2O Project (IHOP_2002) and some preliminary highlights. *Bull. Amer. Meteor. Soc.*, **85**, 253–277, doi:10.1175/BAMS-85-2-253.

——, J. W. Wilson, M. Hagen, T. J. Emerson, J. O. Pinto, D. L. Rife, and L. Grebe, 2011: Radar climatology of the COPS region. *Quart. J. Roy. Meteor. Soc.*, **137** (S1), 31–41, doi:10.1002/qj.747.

Wilks, D., 2006: *Statistical Methods in the Atmospheric Sciences.* 2nd ed. International Geophysics Series, Elsevier, 627 pp.

Wilson, L., M. J. Manton, and S. T. Siems, 2012: Relationship between rainfall and weather regimes in south-eastern Queensland, Australia. *Int. J. Climatol.*, **33**, 979–991, doi:10.1002/joc.3484.

Wulfmeyer, V., and Coauthors, 2011: The Convective and Orographically-induced Precipitation Study (COPS): The scientific strategy, the field phase, and research highlights. *Quart. J. Roy. Meteor. Soc.*, **137** (S1), 3–30, doi:10.1002/qj.752.

Zhang, J., K. Howard, and J. J. Gourley, 2005: Constructing three-dimensional multiple-radar reflectivity mosaics: Examples of convective storms and stratiform rain echoes. *J. Atmos. Oceanic Technol.*, **22**, 30–42, doi:10.1175/JTECH-1689.1.

Zipser, E. J., and K. R. Lutz, 1994: The vertical profile of radar reflectivity of convective cells: A strong indicator of storm intensity and lightning probability? *Mon. Wea. Rev.*, **122**, 1751–1759, doi:10.1175/1520-0493(1994)122<1751:TVPORR>2.0.CO;2.

Zuidema, P., 1998: The 600–800-mb minimum in tropical cloudiness observed during TOGA COARE. *J. Atmos. Sci.*, **55**, 2220–2228, doi:10.1175/1520-0469(1998)055<2220:TMMITC>2.0.CO;2.